

SPACE SCIENCES LABORATORY

N72-33764

CASE FILE COPY

PLANETARY X-RAY EXPERIMENT

Dr. Kevin Hurley

Dr. Kinsey A. Anderson

Final Report

NGR 05-003-458

Space Sciences Laboratory Series 13 Issue 78

UNIVERSITY OF CALIFORNIA, BERKELEY

Space Sciences Laboratory
University of California
Berkeley, California 94720

SUPPORTING RESEARCH FOR OUTER PLANETS MISSION -
EXPERIMENT DEFINITION PHASE

Dr. Kevin Hurley
Dr. Kinsey A. Anderson

Final Report
NGR 05-003-458

SUMMARY

The purpose of the work carried out under NASA Headquarters grant NGR 05-003-458 was two-fold:

- 1) To examine models of Jupiter's magnetosphere with the particular purpose of predicting the X-ray flux that would be emitted in auroral or radiation zone processes.
- 2) To investigate the various types of X-ray detection for energy resolution, efficiency, reliability, and background, and then from the model fluxes to decide under what models Jovian X-rays could be detected.

We have found that the proportional counter is best suited for an outer planet mission because of its overall simplicity, the achievability of low background, the ease of attaining large areas at low mass with a counter of modest size, and its suitability for the MJS mission. It is concluded that there is a high probability that Jovian X-rays will be detected at distances up to 1 A.U. from the planet.

The report consists of a discussion of the models used to predict X-ray fluxes and the instrumentation most suited to measure them. Much of the work reported here was carried out by Dr. Kevin Hurley.

FINAL REPORT FOR NGR 05-003-458 (SUPPORTING RESEARCH FOR
OUTER PLANETS MISSION - EXPERIMENT DEFINITION PHASE)

As the planet Jupiter is known to possess an active magnetosphere, and Saturn is strongly suspected to have one, these two planets should be sources of X-radiation, produced by bremsstrahlung from energetic electrons which precipitate into the planetary atmospheres. A study of planetary X-rays therefore gives information about particle fluxes, and constitutes a powerful tool for the remote sensing of magnetospheric dynamics. We had made previous estimates of Jupiter's X-ray flux, based on theoretical considerations (1). Our goal, under NGR 05-003-458, was

First, to revise the estimates of the Jovian X-ray fluxes, using any relevant new information, and to generate similar estimates for Saturn.

Second, using these new estimates, to determine the best type of X-ray experiment, for a Grand Tour or MJS-type spacecraft, which could detect these fluxes.

Third, to compare the best MJS experiment with other types of experiments, such as balloon, rocket, and satellite X-ray detectors, to determine whether a flyby experiment offered significant advantages over these other types.

We have summarized our work on these three phases in the following three sections.

I. MODELS FOR PLANETARY X-RAY EMISSION

There is at present no data on the spectrum of kilovolt electrons in the Jovian magnetosphere. Therefore, in order to calculate the flux of Jovian X-rays, models must be constructed which allow the known terrestrial electron spectra to be scaled to the Jovian magnetosphere. Once the assumed Jovian electron spectrum has been calculated, the X-ray flux follows by applying the formulas for bremsstrahlung cross sections. This is explained in Appendix A.

MODEL IA

This model is based on the assumption that the ultimate source of energy for all terrestrial auroral phenomena is derived from the solar wind particle energy. If the same fraction of Jupiter's energy input goes into precipitating electron fluxes as the earth's, the Jovian fluxes can be found by scaling the terrestrial fluxes by a factor which depends on the intercepted solar wind energies.

In the cases of both the earth and Jupiter, the planetary magnetic fields do not extend out into space indefinitely; they are balanced at some point by the pressure of the solar wind. Thus if n , m , and v are the number density, particle mass, and velocity of the solar wind, and B_d is the planetary dipole field strength, the boundary will occur where

$$2nmv^2 \cos^2 \psi = \frac{(2B_d)^2}{8\pi}$$

Here, ψ is the angle between v and a normal to the boundary, and the field just inside the boundary has been increased to twice the dipole

value, due to currents flowing along the boundary. Since Ψ depends, in turn, upon the shape of the boundary, the above equation must be solved by iterative techniques, except at the subsolar point, where $\Psi = 0$. Thus if M is the planetary magnetic moment, and r is the distance from the center of the planet (assumed to be the center of dipole), the radius of the magnetosphere at the subsolar point is

$$r_0 = (M^2/4\pi n m v^2)^{1/6}$$

The quantity of interest is the cross sectional area presented to the solar wind, or the cross section in the dawn-dusk meridian. Detailed calculations (2) have shown that this cross section is approximately elliptical with semiminor and semimajor axes r_0 and $1.4 r_0$, respectively. Thus the cross sectional areas should scale as r_0^2 and the scaling factor relating Jovian to terrestrial intercepted energy becomes, in this case

$$\frac{n_J m v^3 r_{0J}^2}{n_E m v^3 r_{0E}^2} = \left[\frac{M_J R_E^2}{M_E R_J^2} \right]^{2/3} = 150$$

where the subscripts J and E refer to Jupiter and the earth, and R is the distance between the planet and the sun. It has been assumed that the solar wind velocity is the same at Jupiter as at the earth, while the number density decreases as $1/R^2$. M_J has been taken to be 4×10^{30} gauss-cm³, or $\sim 5 \times 10^4 M_E$. r_{0J} is then approximately $50 R_J$.

The total power intercepted by the earth's magnetosphere is about 10^{20} ergs/sec, of which roughly 10^{18} ergs/sec goes into auroral phenomena of all kinds. Jupiter, then, should intercept 1.5×10^{22} ergs/sec and use 1.5×10^{20} ergs/sec for its auroral phenomena, according to this model. (For comparison, the average power dissipated in Jovian

decimetric and decametric radiation is about 10^{16} ergs/sec.) If the energy spectrum of precipitating electrons is now taken to be

$$\frac{dN}{dE} = C e^{-E/E_0} \text{ electrons/cm}^2 \text{ sec keV}$$

(see Appendix A), the total energy flux precipitated is

$$\int_0^{\infty} E \frac{dN}{dE} dE = C E_0^2 \text{ keV/cm}^2 \text{ sec.}$$

A question remains as to the area into which electrons are precipitated. Although the earth's auroral zones are generally taken to be those areas between latitudes 65° and 70° in both the northern and southern hemispheres (the boundary between open and closed field lines), precipitation at any given time will involve only about 1% of this area, or $3 \times 10^{15} \text{ cm}^2$ over one hemisphere. If the same latitudes are assumed to define the Jovian auroral zones, and if the precipitation occurs over the same percentage of the area, the size of the precipitating region will scale as the square of the planetary radius. [However, see (3) for a different approach which gives a slightly lower value.] Taking $r_J = 7.1 \times 10^9 \text{ cm}$ as the radius of Jupiter, and $r_E = 6.3 \times 10^8 \text{ cm}$ as the radius of the earth, the precipitating region on Jupiter is found to be 110 times larger than the area on the earth, or $3 \times 10^{17} \text{ cm}^2$. Although electron precipitation shows different time structure on the earth's day and night sides, the total X-ray energy is approximately the same for both sides; thus these calculations should apply to both sides of a planet. The total power in electron fluxes becomes $A_J C_J E_{0J}^2$ for Jupiter, and $A_E C_E E_{0E}^2 = 2.1 \times 10^{25}$

keV/sec for the earth, where A_E and A_J are the areas of the precipitating regions on the earth and Jupiter and the spectral parameters C and E_0 have been assumed to be different for the two planets. Now, scaling the power dissipated by the ratio of the intercepted energies,

$$A_J C_J E_{0J}^2 = 150 A_E C_E E_{0J}^2 = 3.15 \times 10^{27} \text{ keV/sec.}$$

From Appendix A, Formula IA, the X-ray spectrum at the earth at MJS launch, when Jupiter is 8.25×10^{13} cm away, is

$$\frac{dh_{IA}(\hbar\omega)}{d(\hbar\omega)} = 8.83 \times 10^{-8} \frac{e^{-\hbar\omega/E_{0J}}}{\hbar\omega} \text{ X-rays/cm}^2 \text{ sec keV.}$$

This spectrum is plotted in Figure 1, for various values of the e-folding energy E_{0J} .

MODEL IB

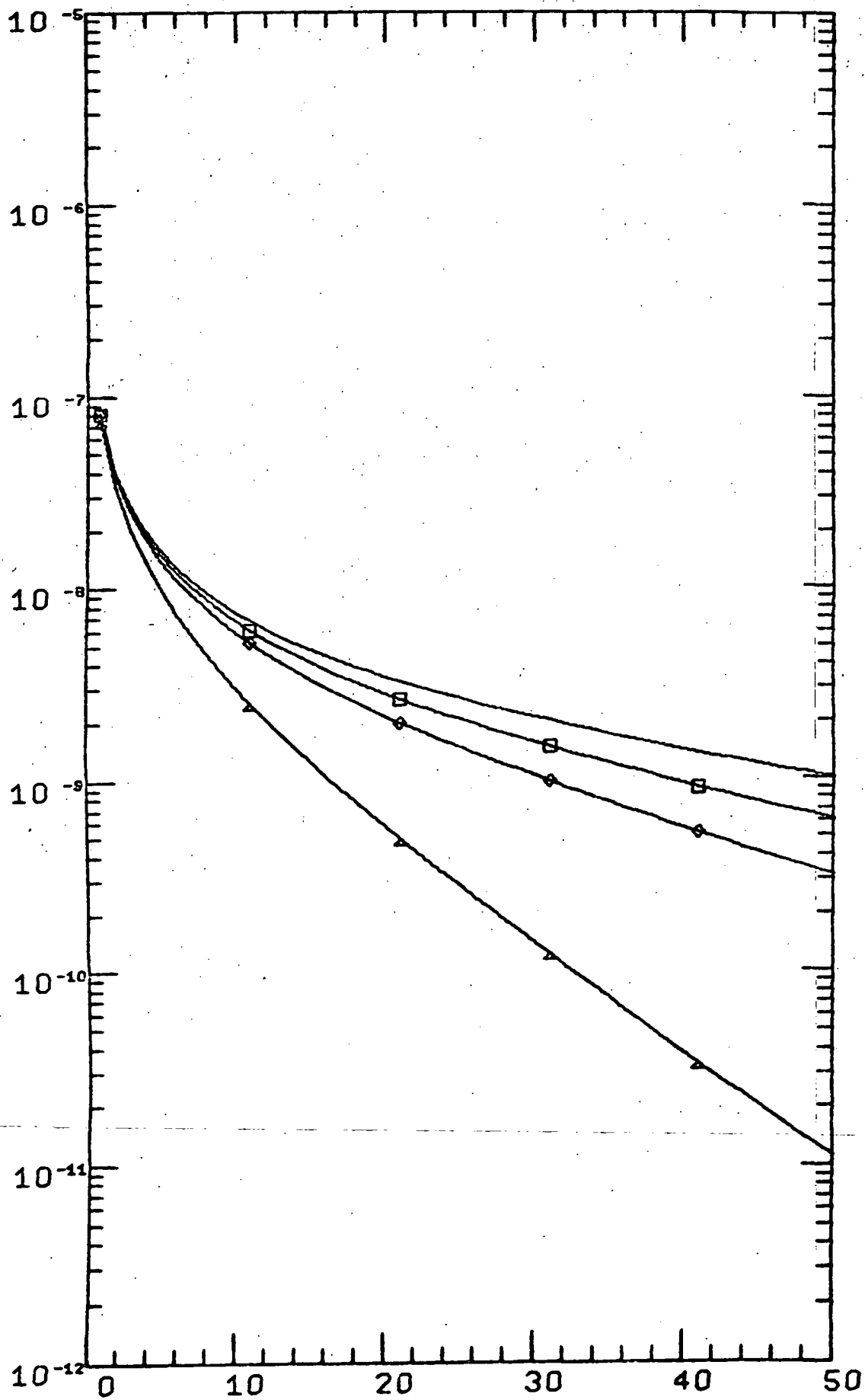
One objection which can be raised to Model IA is that it is a steady state model: energy flows into and out of the magnetosphere without being stored. In reality, there is good evidence that the magnetic field lines in the earth's auroral zones connect to a highly diamagnetic sheet of plasma which stretches out in the antisolar direction behind the earth (4, 5). Thus the electron energy density in this region is comparable to the magnetic field energy density, and energy is indeed stored in the tail of the magnetosphere. Assuming that this represents an upper limit for Jupiter as well as for the earth, the Jovian electron energy density may be scaled by the ratio of the magnetic field energy densities. If $u = c\sqrt{\frac{2E}{mc^2}}$ is the velocity of an electron with kinetic energy E and

DNIA/DHW (PHOTONS/CM2 SEC KEU)

RJIG = 3.00E+17 CM2

DEJ = 8.25E+13 CM

DEL(E0=10), DIAMOND(E0=30), SQUARE(E0=50), BLANK(E0=100)



HW, KEU

Figure 1

and rest energy mc^2 , the energy density of an exponential electron spectrum $\frac{dN}{dE} = C e^{-E/E_0}$ is given by

$$\int_0^{\infty} \frac{E}{u} C e^{-E/E_0} dE = \frac{C}{c} \sqrt{\frac{mc^2}{2}} E_0^{3/2} \Gamma(3/2)$$

where Γ is the gamma function. The use of the nonrelativistic velocity is justified by the fact that, for the E_{0J} to be used in this expression, the contribution at energies $E \sim mc^2$ is very small.

The scaling factor is B_J^2/B_E^2 , where B_J and B_E are the magnetic field strengths at corresponding points on Jupiter and the earth; assuming dipole fields, this becomes

$$\left(\frac{M_J}{r_J^3} \frac{r_E^3}{M_E} \right)^2 = 2.5 \times 10^3.$$

Thus

$$C_J E_{0J}^{3/2} = 2.5 \times 10^3 C_E E_{0E}^{3/2}$$

or

$$C_J E_{0J}^2 A_J = 2.5 \times 10^3 C_E E_{0E}^{3/2} \sqrt{E_{0J}} A_J = 1.66 \times 10^{30} \sqrt{E_{0J}}.$$

From Appendix A, formula IA, the X-ray spectrum at the earth is

$$\frac{dn_{IB}(\hbar\omega)}{d(\hbar\omega)} = 4.66 \times 10^{-5} \sqrt{E_{0J}} \frac{e^{-\hbar\omega/E_{0J}}}{\hbar\omega} \text{ X-rays/cm}^2.$$

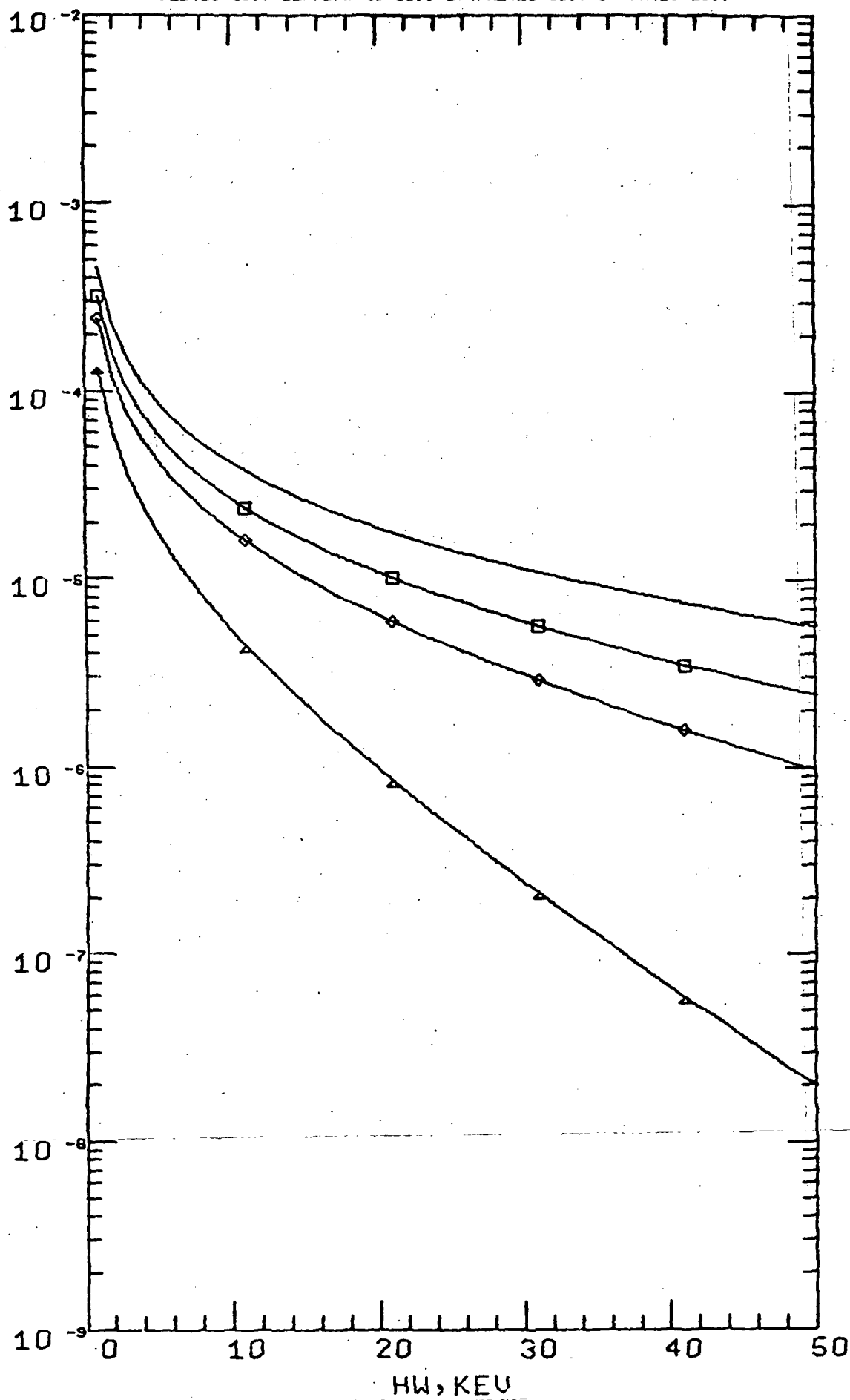
This spectrum is plotted in Figure 2, for various values of the electron e-folding energy E_{0J} .

DNIS/DHW (PHOTONS/CM2 SEC KEV)

AJIS = 3.00E+17 CM2

DEJ = 8.26E+13 CH

DEL(E0=10), DIAMOND(E0=30), SQUARE(E0=50), BLANK(E0=100)



HW, KEV

Figure 2

MODEL II

Finally, it should be noted that there are Jovian phenomena, such as the decametric radiation, which have no counterpart on earth. Expanding on the calculations of Warwick (6), assuming that this is electron gyro-radiation, suppose that the flux density observed at the earth due to decametric radiation is ϕ keV/cm² sec Hz at a frequency f (Hz), and that the signal has a bandwidth Δf (Hz). If the radiation is beamed into a solid angle Ω (sterad), and the earth is a distance D (cm) away, the total power radiated by the source is

$$\phi \Delta f \Omega D^2 \text{ keV/sec.}$$

A single electron of energy E (keV) radiates a total power $4 \times 10^{-9} B^2 \sin^2 \alpha$ keV/sec due to gyroradiation, where B is the magnetic field strength in gauss, and α is the angle between \vec{B} and the electron velocity \vec{u} . In an electron spectrum $\frac{dN}{dE}$ electrons/cm² sec keV, the total power radiated/unit volume is

$$4 \times 10^{-9} B^2 \sin^2 \alpha \int_0^{\infty} \frac{E}{u} \cdot \frac{dN}{dE} dE \text{ keV/cm}^3.$$

Taking $\frac{dN}{dE} = C_J e^{-E/E_{0J}}$ electrons/cm² sec keV, and $u = C \sqrt{\frac{2E}{mc^2}}$ cm/sec (the nonrelativistic form for the velocity is justified again by the fact that the contribution from the exponential spectrum becomes very small for energies near mc^2 , for the values of E_{0J} used here), the total power radiated per unit volume becomes

$$4 \times 10^{-9} B^2 \sin^2 \alpha \frac{C_J}{c} \sqrt{\frac{mc^2}{2}} E_{0J}^{3/2} \Gamma(3/2).$$

The total volume into which the electrons precipitate is $A_J \Delta R$, where A_J is the area and ΔR the thickness of the precipitation region. Following Warwick (6), the thickness is found by assuming that the bandwidth of the decametric radiation is related to the change in the magnetic field as the electrons move closer to the planet

$$\Delta R = R \frac{\Delta B}{3B} = R \frac{\Delta f}{3f} = \frac{\Delta f}{3 \times 2.8 \times 10^6 B}$$

where R is the planetary radius, ΔB is the change in the field strength, and the expression $f = 2.8 \times 10^6 B$ has been used for the gyrofrequency.

Thus

$$\phi \Delta f \Omega D^2 = 4 \times 10^{-9} B^2 \sin^2 \alpha \frac{C_J}{c} \sqrt{\frac{mc^2}{2}} E_{oJ}^{3/2} \Gamma(3/2) R \frac{\Delta f}{8.4 \times 10^6 B} A_J$$

or

$$C_J E_{oJ}^2 A_J = \sqrt{E_{oJ}} \frac{\phi \Omega D^2}{R B \sin^2 \alpha} 4.5 \times 10^{24} = 1.4 \times 10^{32} \sqrt{E_{oJ}}$$

for Jupiter, using values in (6):

$$\phi = 10^{-19} \text{ watts/m}^2 \text{ Hz} = 6.24 \times 10^{-8} \text{ keV/cm}^2$$

$$\Omega = 8.63 \times 10^{-3} \text{ sterad. (a cone of half-angle } 3^\circ)$$

$$B = 8.9 \text{ gauss}$$

$$D = 4 \text{ A.U.} = 6 \times 10^{13} \text{ cm}$$

$\sin^2 \alpha$ has been taken to be 1, corresponding to a mirroring particle.

From Appendix A, Formula IA, the X-ray spectrum at the earth is

$$\frac{dn_{II}(\hbar\omega)}{d(\hbar\omega)} = 3.92 \times 10^{-3} \sqrt{E_{oJ}} \frac{e^{-\hbar\omega/E_{oJ}}}{\hbar\omega} \text{ X-rays/cm}^2 \text{ sec keV}$$

This is plotted in Figure 3, for various values of the e-folding energy E_{oJ} .

X-RAYS FROM Io

Goldreich and Lynden-Bell (7) have estimated that, since Io is immersed in the Jovian radiation belts, it should be a source of kilovolt X-rays; they give a flux of roughly 10^{-7} X-rays/cm² sec at the earth. Thus this is comparable to the flux of Model IA.

SATURNIAN X-RAYS

There have been reports (8, 9, 10, 11) of sporadic non-thermal radio emission from Saturn; theoretical estimates of Saturn's magnetic moment based on these observations (12, 13, 14, 15), or on general scaling relationships (16, 17) vary widely. For the following section, an intermediate value of $M_S = 2 \times 10^{29}$ gauss-cm³ (or $2.5 \times 10^3 M_E$) is used. This gives a surface field of about 1 gauss at the equator, and a magnetospheric radius of $39 R_S$ at the subsolar point. As the radius of Saturn is $r_S = 9.45 r_E$, the area of the precipitating region should be 2.68×10^{17} cm².

MODEL IA (SATURN)

Following the calculations for the Jovian Model IA, the scaling factor relating Saturnian to terrestrial intercepted energy becomes

$$\left(\frac{M_S R_E^2}{M_E R_S^2} \right)^{2/3} = 9.2, \text{ so } A_{SS} C_{S oS}^2 = 9.2 A_{EE} C_{E oE}^2 = 1.94 \times 10^{26} \text{ keV/sec.}$$

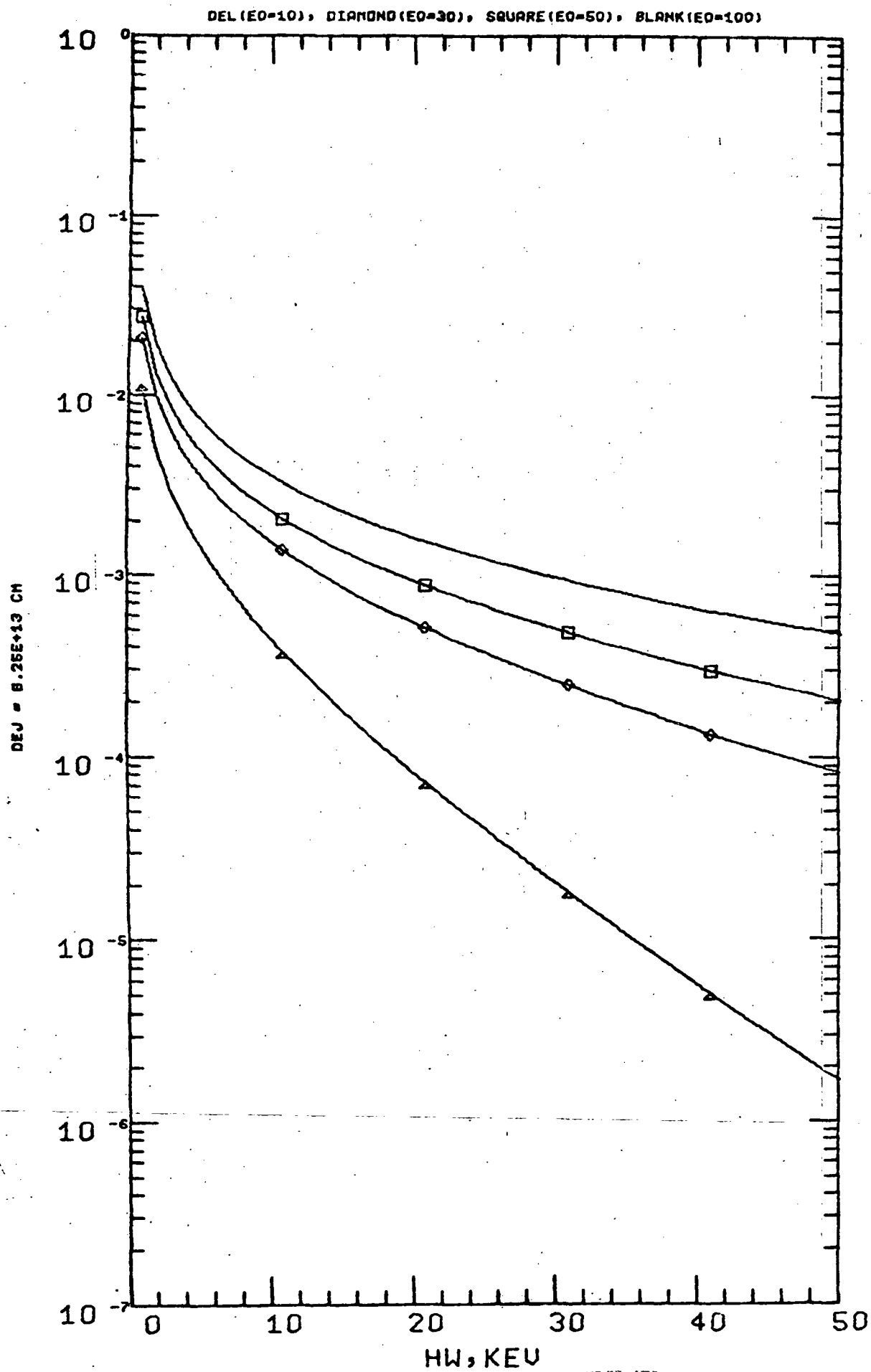


Figure 3

As the distance between Saturn and the earth is 10.5 astronomical units (1.57×10^{14} cm) at MJS launch, the Saturnian X-ray spectrum is about one order of magnitude below the Jovian spectrum, or, from Formula IA, Appendix A,

$$\frac{dn_{IA}(\hbar\omega)}{d(\hbar\omega)} = 1.5 \times 10^{-9} \frac{e^{-\hbar\omega/E_{oS}}}{\hbar\omega} \text{ X-rays/cm}^2 \text{ sec keV}$$

This is plotted in Figure 4, for various values of the e-folding energy E_{oS} .

MODEL IB (SATURN)

Following the calculation for the Jovian Model IB, we obtain a scaling factor

$$\left(\frac{M_S}{r_S^3} \frac{r_E^3}{M_E} \right)^2 = 8.77$$

so

$$C_{S E_{oS}}^{3/2} = 8.77 C_{E_{oE}}^{3/2}$$

or

$$C_{S E_{oS}}^2 A_S = 8.77 C_{E_{oE}}^{3/2} A_S \sqrt{E_{oS}} = 5.20 \times 10^{27} \sqrt{E_{oS}}$$

From Appendix A, Formula IA, the X-ray spectrum at the earth is

$$\frac{dn_{IB}(\hbar\omega)}{d(\hbar\omega)} = 4.03 \times 10^{-8} \sqrt{E_{oS}} \frac{e^{-\hbar\omega/E_{oS}}}{\hbar\omega} \text{ X-rays/cm}^2 \text{ sec keV}$$

at launch. This is plotted in Figure 5, for various values of the e-folding energy E_{oS} .

DNIA/DHW (PHOTON/CM2 SEC KEU)

DES = 1.57E+14 CM

DEL(E0=10), DIAMOND(E0=30), SQUARE(E0=50), BLANK(E0=100)

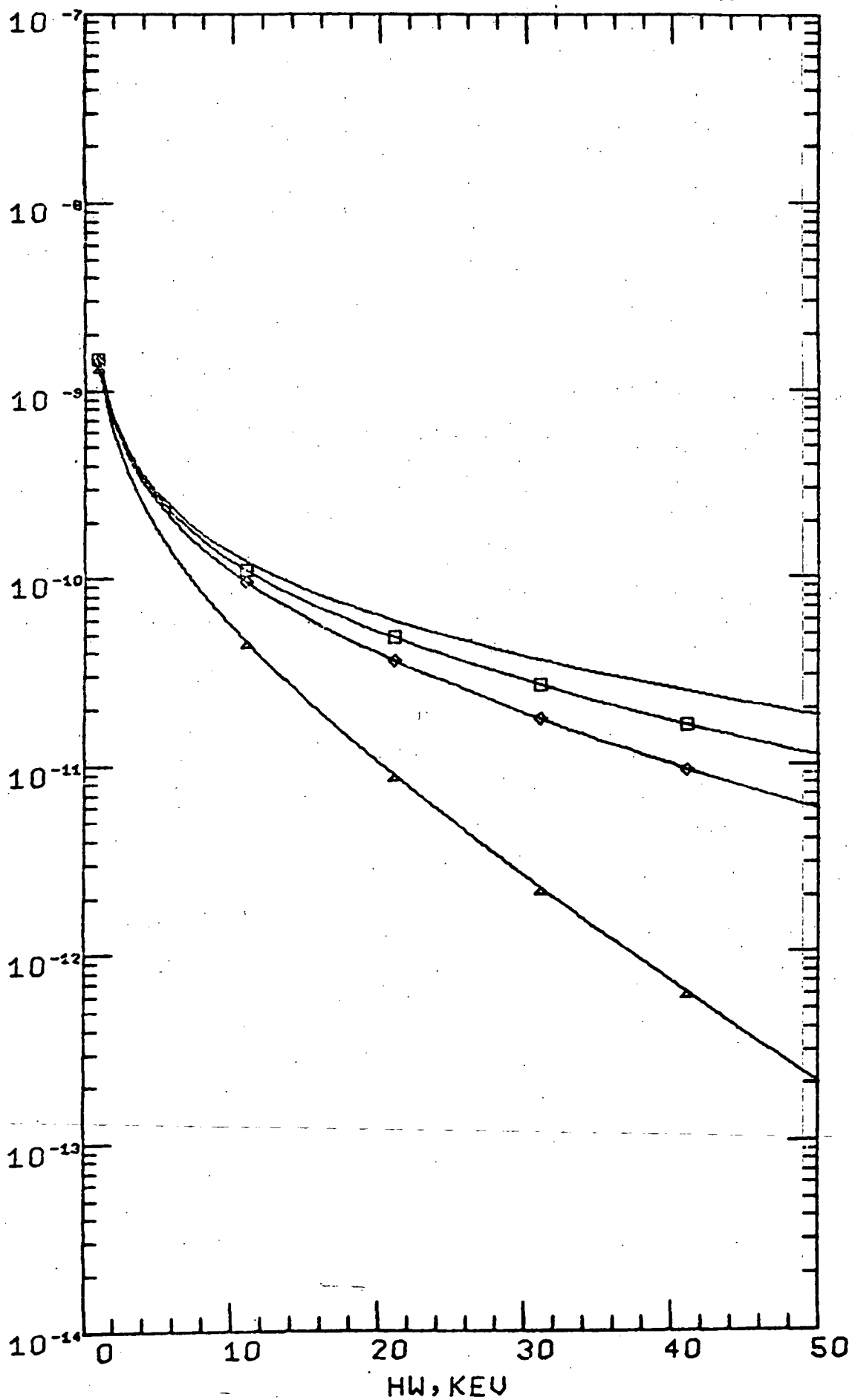


Figure 4

DNIB/DHW (PHOTON/CM2 SEC KEV)

DES = 1.57E+14 CM

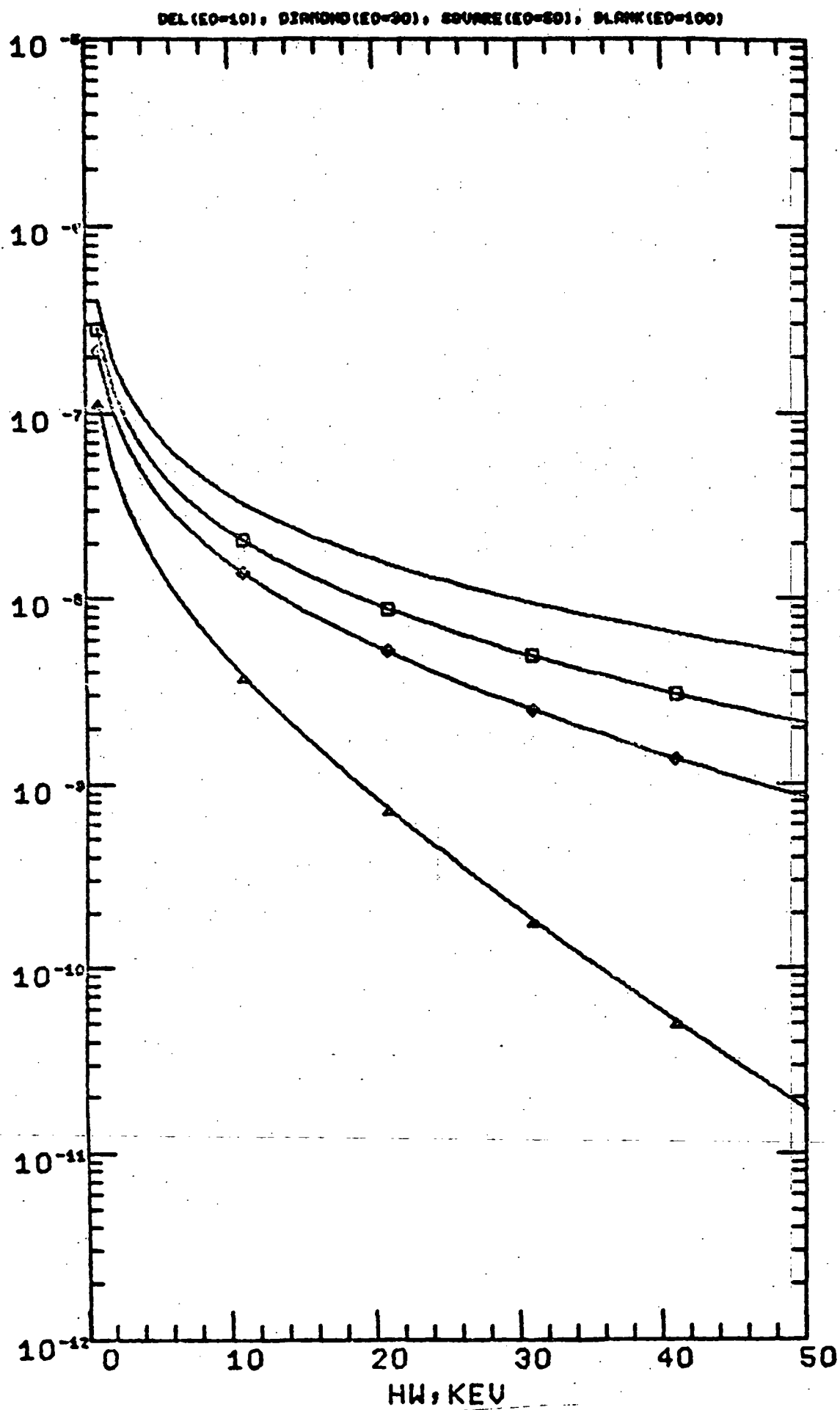


Figure 5

MODEL II (SATURN)

This is based on the same argument as the Jovian Model II. From (18), the value $\phi = 10^{-22}$ watts/m²Hz = 6.24×10^{-11} keV/cm² is used. The value of B is taken to be 2 gauss near the surface of the planet at the poles, and, as a guess, the same value of Ω is used for Jupiter. Thus

$$\begin{aligned} C_S E_{oS}^2 A_S &= 4.5 \times 10^{24} \sqrt{E_{oS}} \frac{\phi \Omega D^2}{R B^2 \sin^2 \alpha} \\ &= 5 \times 10^{30} \sqrt{E_{oS}} \end{aligned}$$

From Appendix A, Formula IA, the X-ray spectrum at the earth is

$$\frac{dn_{II}(\hbar\omega)}{d(\hbar\omega)} = 3.87 \times 10^{-5} \sqrt{E_{oS}} \frac{e^{-\hbar\omega/E_{oS}}}{\hbar\omega} \text{ X-rays/cm}^2 \text{ sec keV.}$$

This is plotted in Figure 6, for various values of E_{oS} .

DNII/DHW (PHOTO, S/CM2 SEC KEU)

DES = 3.57E+14 CM

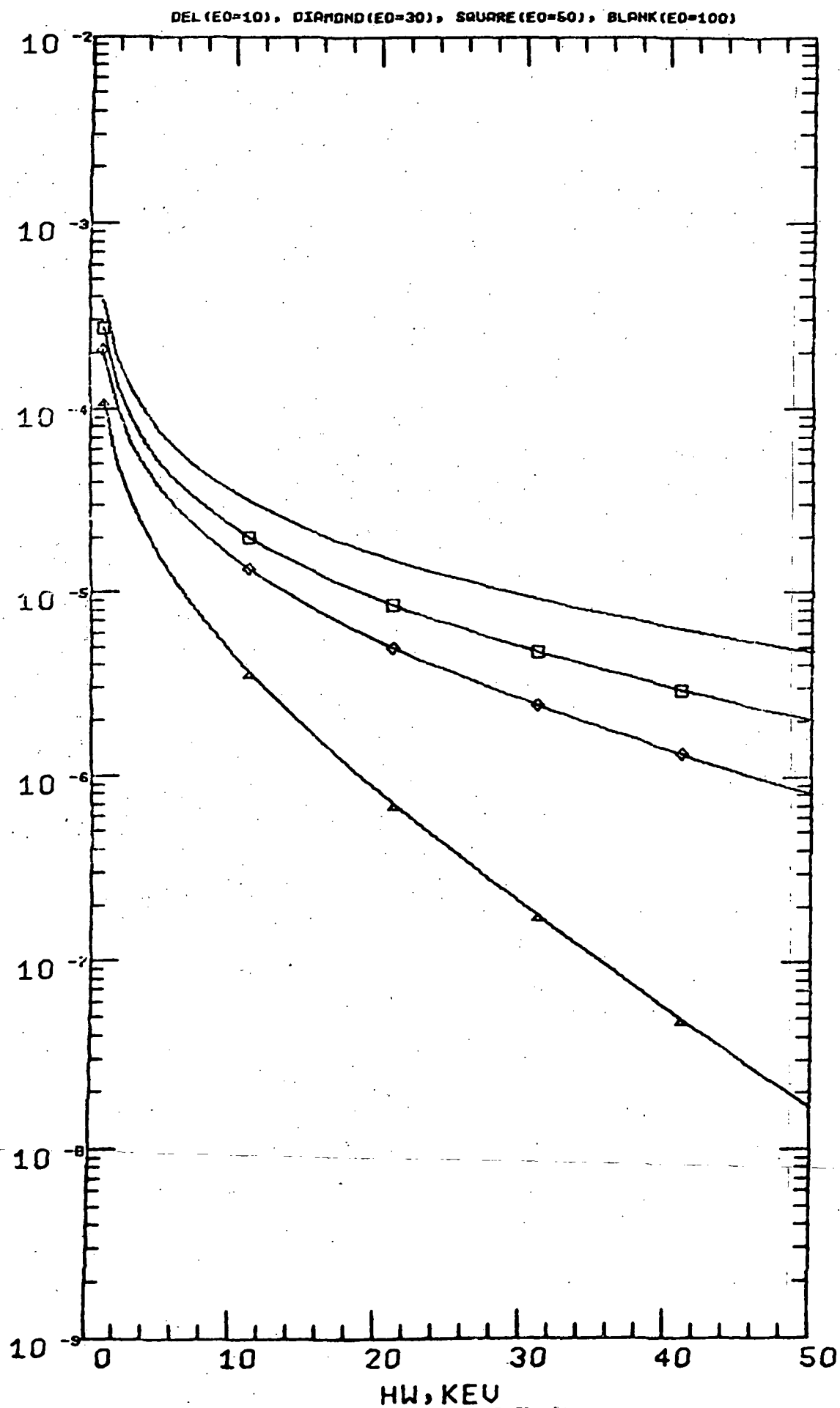


Figure 6

II. INSTRUMENTATION FOR A FLYBY X-RAY EXPERIMENT

Much of the work done for this phase was written up in "Instrument Report: Planetary X-ray Experiment"; we have therefore included this report as Appendix B. As it seemed desirable to measure not only bremsstrahlung X-rays, but also fluorescent X-rays from the satellites of the outer planets (and therefore obtain composition information), we considered the possibility of using very high resolution Si(Li) detectors. Two serious problems were found, however:

- a) In the Grand Tour configuration, radiation damage from both RTG's and planetary trapped radiation would have decreased the useful lifetime of the detectors to less than the mission lifetime.
- b) The background counting rate from the RTG's would be very high. We experimented with Si(Li) detectors and fast rise time pre-amplifiers, attempting to do pulse shape discrimination, which would help to solve the background problem. We concluded that this technique was not feasible, and turned our attention to proportional counters. On the basis of the upper limit calculations in the Instrument Report, we determined that a proportional counter was capable of operating reliably, and with a reasonable background rate, on a Grand Tour type spacecraft.

One point which required further investigation was the problem of Compton electron production in the proportional counter walls by RTG gamma rays. We developed a Monte Carlo program to study this effect, and to improve on the upper limit calculations in the Instrument Report.

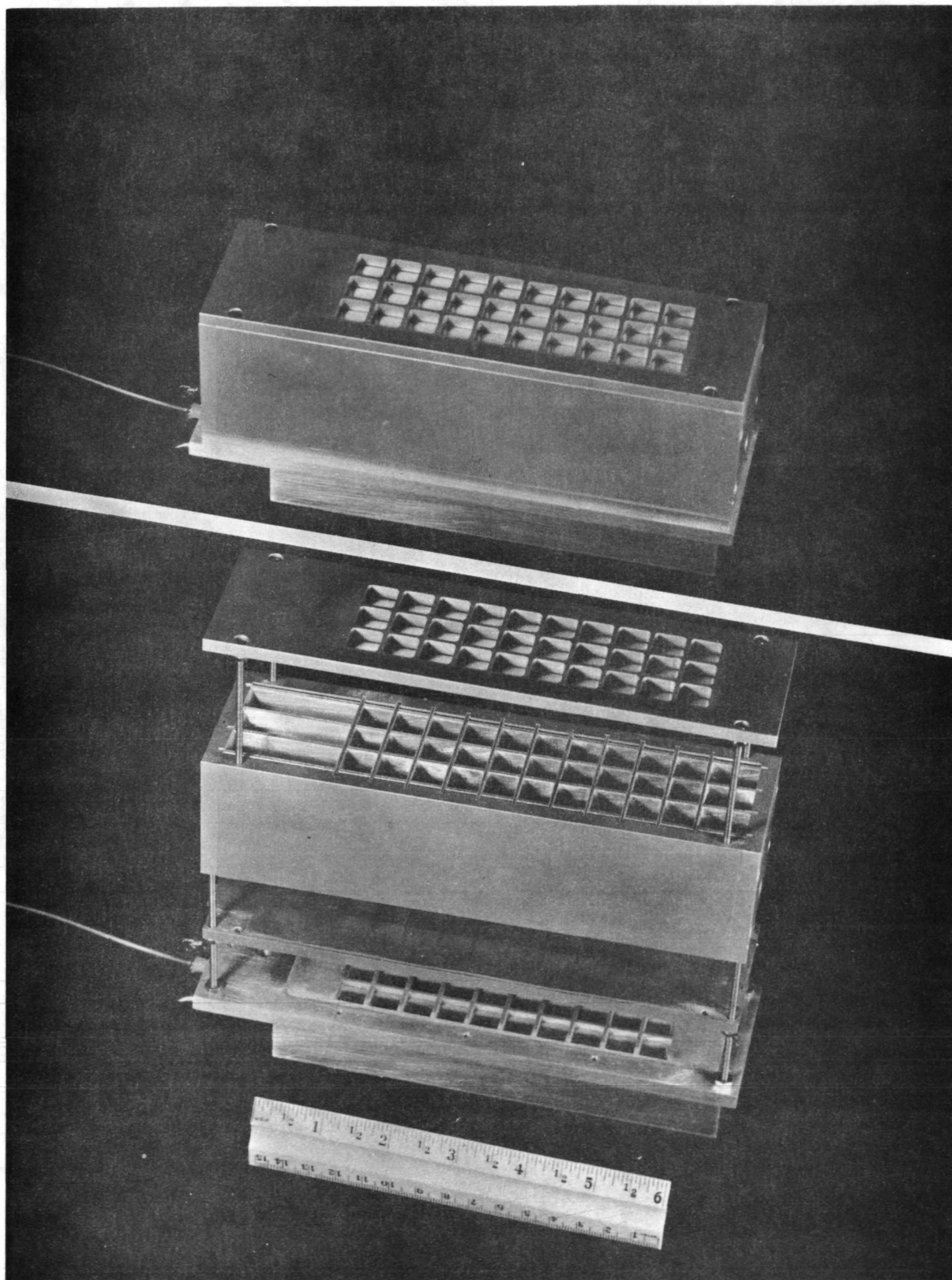


Figure 7

At the same time, we began construction of a prototype detector; this is shown in Figure 7. It consists of a proportional counter with a passive collimator restricting the field of view to about $7^\circ \times 7^\circ$ FWHM and a modulation collimator consisting of 2 electrodeposited tungsten meshes. The purpose of the modulation collimator is to provide X-ray source size information down to about 0.1° . We tested this double collimator with various size light sources; the results of the test are shown in Figure 8. As the collimator is rotated, the detector response is a roughly triangular envelope (the response of the $7^\circ \times 7^\circ$ collimator) containing a series of finer triangles (the modulation collimator response). The peak to valley ratio of the modulation collimator response indicates the source size.

Finally, we tested the prototype detector at JPL, in the presence of the simulated RTG; the results of this test agreed well with the background estimates we had made using the RTG description in the MJS AFO package, in conjunction with our Monte Carlo results.

The detector which we propose to fly on the MJS mission is shown in Figure 9; it is divided into two separate gas chambers for redundancy, and each gas chamber has smaller anticoincidence chambers around the sides to eliminate the Compton electron contribution. We have estimated the total background count rate in this detector to be 2.2 counts/sec on the MJS spacecraft.

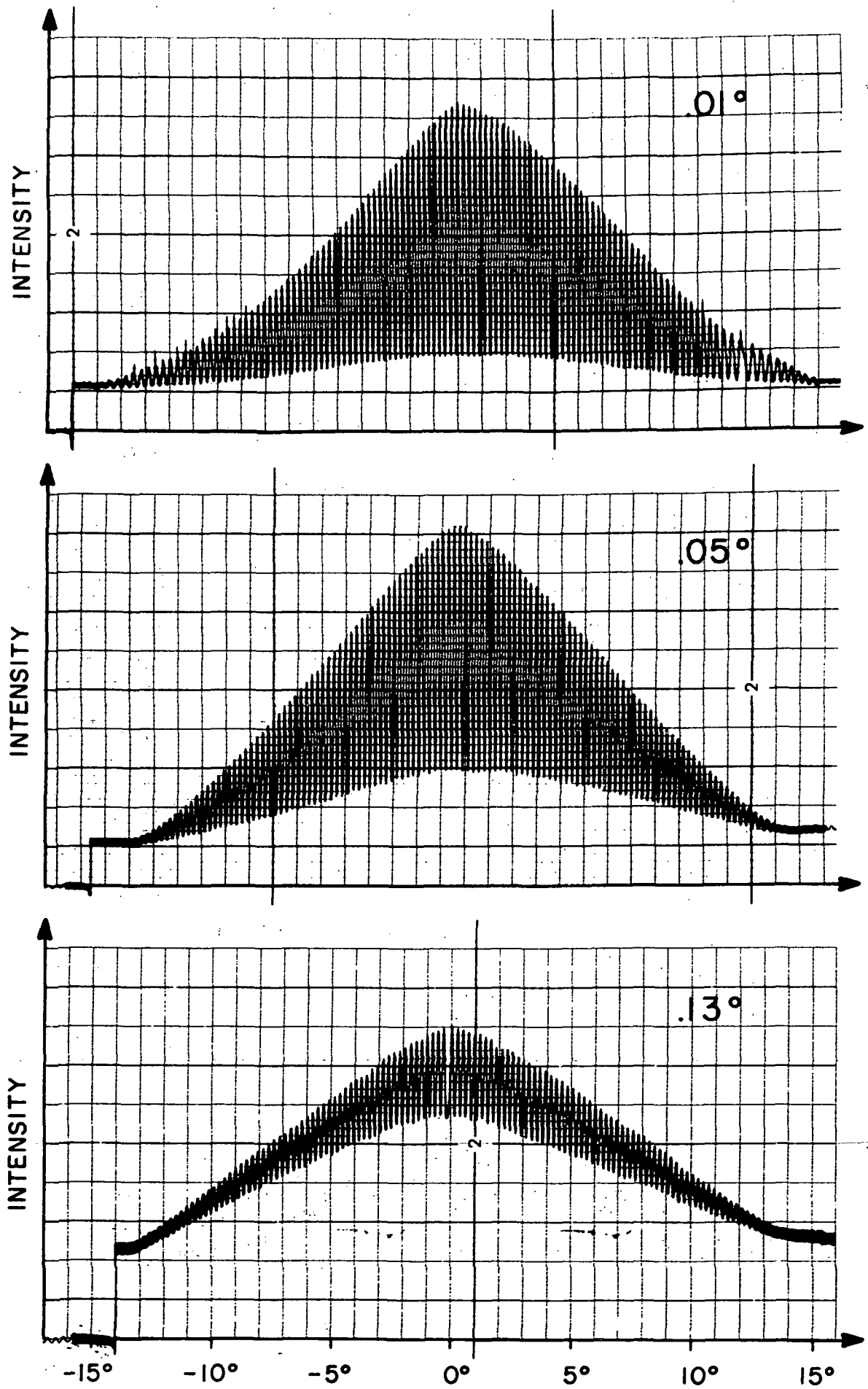
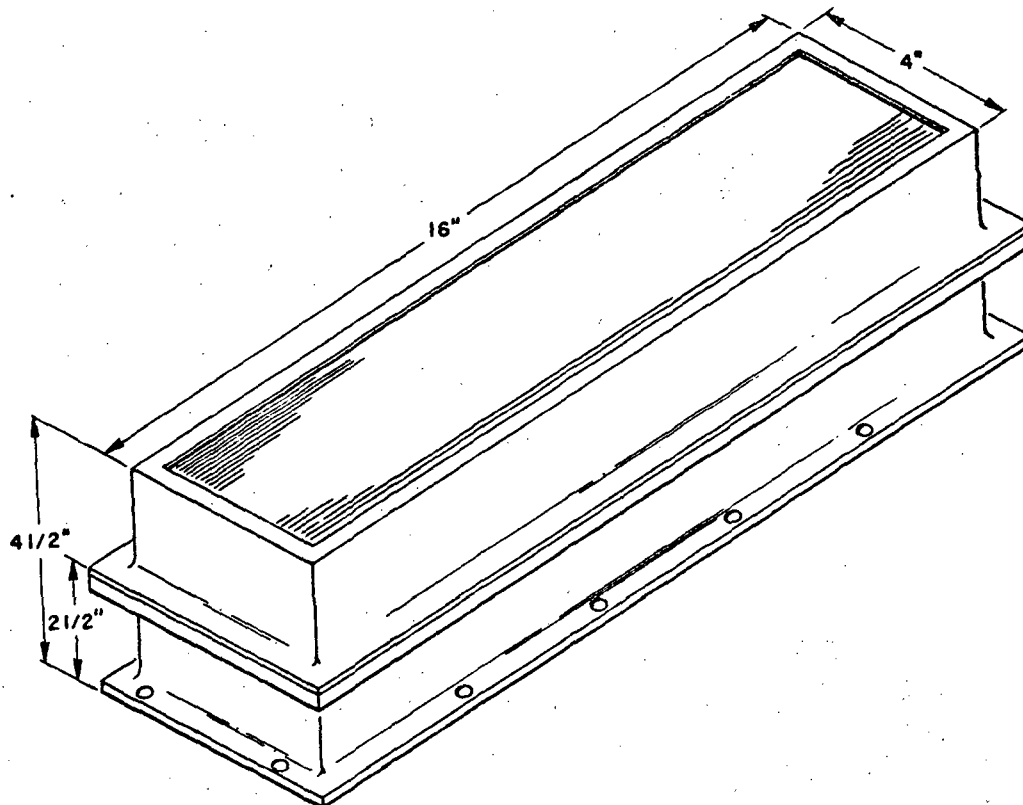


Figure 8



WIRE SUSPENSION DETAIL

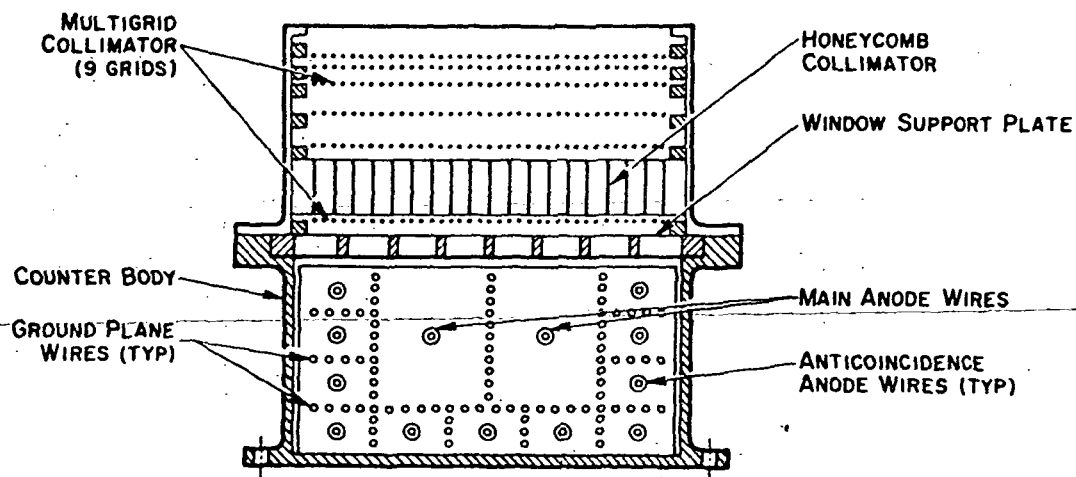
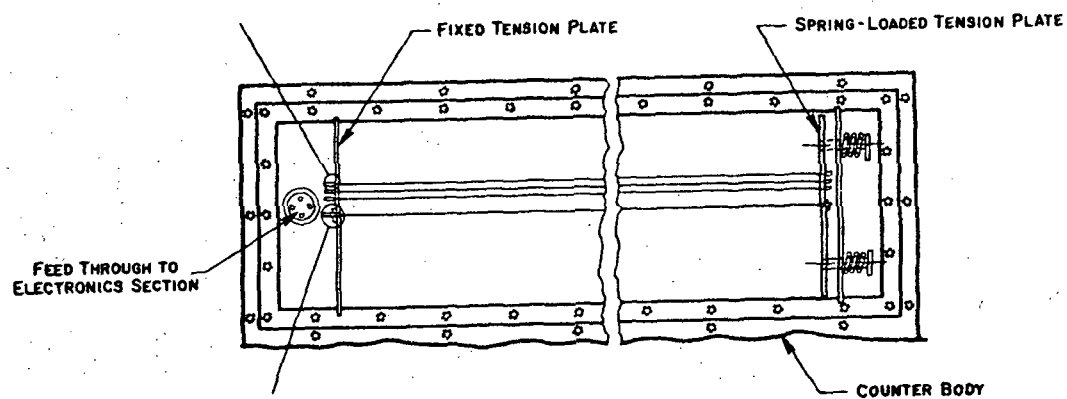


Figure 9

III. STATISTICS AND METHODS OF OBSERVING JUPITER X-RAYS

Let n be the number of counts/second received by a given detector in some energy range due to an X-ray source (formula 2A of Appendix A), and let B be the number of counts/sec, due to background in the same energy range. In a time T , it is desired to measure both n and B , and to derive n with the maximum accuracy. The count rate is thus $n + B$ during the source observation, and B during the background observation. Suppose a fraction α of the time T is devoted to the source, so that

$$(n + B) \alpha T \pm [(n + B) \alpha T]^{1/2}$$

counts are received during this observation period. Then a time $(1 - \alpha)T$ is left for the background observation, and

$$B(1 - \alpha)T \pm [B(1 - \alpha)T]^{1/2}$$

counts are received during that period. The number of source counts is derived by multiplying the number of background counts by $\frac{\alpha}{1 - \alpha}$ and subtracting, to get

$$n \alpha T \pm \left\{ (n + B) \alpha T + \frac{\alpha^2}{1 - \alpha} BT \right\}^{1/2}$$

The maximum accuracy of this quantity is obtained for the minimum value of the quantity

$$\left\{ (n + B) \alpha T + \frac{\alpha^2}{1 - \alpha} BT \right\}^{1/2} / n \alpha T$$

and this is obtained for

$$\alpha = \frac{\left(\frac{n + B}{B}\right)^{1/2}}{1 + \left(\frac{n + B}{B}\right)^{1/2}} .$$

Requiring the number of source counts to be 3 standard deviations above zero (for 99% confidence) means that

$$T = 9 \left\{ \frac{n + B}{n^2} \frac{1}{\alpha} + \frac{B}{n^2} \frac{1}{1 - \alpha} \right\}$$

We will consider only the case $n \ll B$, to derive an upper limit to the time needed. For this case $\alpha \approx 1 - \alpha \approx 1/2$, i.e., equal times are needed for source and background observations; the total time needed is

$$T = 36 \frac{B}{n^2}$$

Alternatively, in a given time T , the minimum detectable count rate is

$$n = 6 \left(\frac{B}{T} \right)^{1/2}$$

If the detector area is A_d , and the average efficiency over the energy range of interest is ϵ , the minimum detectable flux is

$$j = \frac{6}{\epsilon A} \left(\frac{B}{T} \right)^{1/2}$$

Using these formulas, we have considered many possible methods for observing the models of Jovian X-ray emission discussed in Section I. The most sensitive of these are the experiments which operate outside the earth's atmosphere, in the energy range below about 30 keV; three of them are explained below, and summarized in Table I.

SATELLITE PROPORTIONAL COUNTER

This is the AS&E experiment on the SAS-A (UHURU) satellite (19, 20). The satellite is spin stabilized, with the spin axis reoriented every day; the instrument is collimated to $5^\circ \times 5^\circ$ FWHM, so the duty cycle for observing any given source is $10^\circ/360^\circ = 0.028$. The response pattern

Table 1

TYPE OF EXPERIMENT	ENERGY RANGE, keV	DETECTOR AREA-EFFICIENCY PRODUCT, cm ²	OBSERVING TIME, SECS.	BACKGROUND COUNT RATE, COUNTS/SEC.	MINIMUM DETECTABLE FLUX, COUNTS/cm ² sec	CAN EXPERIMENT DETECT JUPITER FLUXES OF		
						MODEL IA?	MODEL IB?	MODEL II?
SATELLITE PROPORTIONAL COUNTER	1.2 - 20	~84	600	20	5×10^{-3}	NO	NO	YES, IF $E_0 > 20$ keV
SATELLITE GRAZING INCIDENCE TELESCOPE	1 - 4	20	5×10^4	.001	3.75×10^{-3}	NO	YES, IF $E_0 > 50$ keV	YES
				.625	1.06×10^{-3}	NO	YES, IF $E_0 > 15$ keV	YES
MJS PROPORTIONAL COUNTER	2 - 30	15	5×10^4	2.2	5.7×10^{-3}	NO	NO	YES, IF $E_0 > 25$ keV
			See last 3 columns		See last 3 columns	YES, IN A TIME ≤ 11 HRS.	YES, IN A TIME $\leq .01$ sec.	YES, IN A TIME $\leq 10^{-6}$ sec.

of the collimator is triangular, so the total observing time must be multiplied by $1/2$ to obtain the effective time. As the earth occults any given source for a total of 12 hrs/day as seen from the satellite, the effective time available on a source is $(12 \text{ hrs})(0.028)(1/2) = 0.168 \text{ hrs}$, or 10 minutes. The area-efficiency product is $\geq 840 \text{ cm}^2 \times 10\% = 84 \text{ cm}^2$. The actual efficiency function $\epsilon(\theta, \omega)$ used in Formula 2A is given in the literature.

SATELLITE GRAZING INCIDENCE TELESCOPE

This experiment is the AS&E grazing incidence telescope to be flown on HEAO-C (21). It is capable of 2 arc second resolution over a 1° field of view; since the disc of Jupiter subtends about 50 arc seconds, the telescope could operate in two different modes. First, a mapping mode, in which the disc is scanned one resolution element at a time, until all $(50/2)^2 = 625$ elements have been scanned; second, simply an X-ray detection mode, where all 625 elements are scanned at once.

In the mapping mode [referred to as the point source mode in (21)], each resolution element gives 50 background counts in an observing period of 5×10^4 seconds (14 hours), for a background counting rate of 10^{-3} counts/second/resolution element. Using equal observing times for Jupiter and background, the total observing time must be divided into $2 \times 625 = 1250$ equal segments, or 40 seconds/segment, during which a resolution element will contribute 0.04 counts. If we require the total probability of a random error simulating a Jupiter X-ray event to be 0.01 for the 625 Jupiter observations, Poisson statistics may be used to find the required number of counts in any Jupiter segment; for a mean of 0.04, three counts are needed for 1.6×10^{-5} probability ($= 0.01/625$) of random simulation.

The sensitivity derived here for the mapping mode is much less than the sensitivity given in (21), where it was assumed that the background was well known, and that a total of 5×10^4 secs would be devoted to a single resolution element. This type of observation would be used if, for example, it were desired to correlate an X-ray source with an optical source whose position were well known.

In the detection mode, the total observing time would be divided into just two segments - Jupiter and background. The background counting rate would be 0.625 counts/second. Dividing the time equally between background and Jupiter, the total number of counts in a segment would be 1.5×10^4 , so Gaussian statistics may be used, and the formulas derived at the beginning of this section may be used.

MJS SPACECRAFT PROPORTIONAL COUNTER

This is a Xenon-filled counter, as described in Section III and Appendix B, with an area-efficiency product of 15 cm^2 . It has a modulation collimator which makes possible the mapping of a planet in X-rays to about $1/10^\circ$; at entry into the Jovian magnetosphere, then, its resolution is comparable to the grazing incidence telescope operating in earth orbit. Two cases are considered: the sensitivity of the counter at launch, 5.5 A.U. from Jupiter, and the sensitivity just before entry into the magnetosphere, 0.02 A.U. from Jupiter. So that this experiment can be compared to the grazing incidence telescope, the observing time has been taken to be 14 hours, for the 5.5 A.U. case. At 0.02 A.U., all models become detectable, and the only question is the amount of time needed; this is tabulated in the last three columns of Table I.

CONCLUSION

As the table shows, the most sensitive earth-based detector is the HEAO grazing incidence telescope; by comparison, the MJS proportional counter is not particularly sensitive if used near the earth. The overwhelming advantage to the MJS experiment is its ability to get very close to Jupiter, where the X-ray fluxes can be observed in short integration times. If simply the detection of Jovian X-rays were desired, this would be theoretically possible for a number of near earth experiments; but if time variations, detailed mapping, and both dayside and nightside observations are required, it is absolutely essential to use a flyby experiment.

REFERENCES

- 1) Hurley, K.: A Search for X-Rays from the Planet Jupiter, Ph.D. Thesis, University of California Department of Physics, Berkeley, 1970.
- 2) Mead, G. D., and Beard, D. B.: Shape of the Geomagnetic Field Solar Wind Boundary, *J. G. R.*, 69, (7), 1169, 1964.
- 3) Brice, N. M., and Ioannidis, G. A.: The Magnetospheres of Jupiter and Earth, *Icarus*, 13, (2), 173, 1970.
- 4) Anderson, K. A.: Relation of Energetic Particles in the Plasma Sheet to the Auroral Zone, in *Atmospheric Emissions*, p. 327, Van Nostrand Reinhold Pub. Co., New York, N. Y., 1969.
- 5) Chase, L. M.: Evidence that the Plasma Sheet is the Source of Auroral Electrons, *J. G. R.*, 74, (1), 348, 1969.
- 6) Warwick, J. W.: Particles and Fields Near Jupiter, NASA Contractor Report CR 1685, 1970.
- 7) Goldreich, P., and Lynden-Bell, D.: Io, A Jovian Unipolar Inductor, *Ap. J.*, 156, 59, 1969.
- 8) Drake, F. D.: Microwave Spectrum of Saturn, *Nature*, 195, (4844), 893, 1962.
- 9) Rose, W. K., Bologna, J. M., and Sloanaker, R. M.: Linear Polarization of the 3200 Mc/sec Radiation from Saturn, *Phys. Rev. Let.*, 10, (4), 123, 1963.
- 10) Smith, A. G., Lebo, G. R., Six, N. F. Jr., Carr, T. D., Bollhagen, H., May, J., and Levy, J.: Decameter Wavelength Observations of Jupiter - the Apparitions of 1961 and 1962, *Ap. J.*, 141, 457, 1965.
- 11) Carr, T. D., Smith, A. G., Bollhagen, H., Six, N. F. Jr., and Chatterton, N. E.: Recent Decameter Wavelength Observations of Jupiter, Saturn, and Venus, *Ap. J.*, (134), 105, 1961.
- 12) Zheleznyakov, V. V.: On the Configuration of the Magnetic Field of Saturn, *Soviet Astronomy-AJ*, 8, (5), 765, 1965.
- 13) Zlotnik, E. Ya.: The Influence of Saturn's Rings on its Exosphere and Magnetic Field, *Soviet Astronomy-AJ*, 11, (3), 462, 1967.
- 14) Haffner, J. W.: The Calculated Environment of the Planet Saturn, Space Division, North American Rockwell Corp., SD 70-561, 1970.
- 15) Haffner, J. W.: Magnetospheres of Jupiter and Saturn, *AIAA Journal*, 9, (12), 2422, 1971.

- 16) Moroz, V. I.: Physics of Planets, "Nauka" Press, Moscow, 1967;
NASA Technical Translation TT F-515, 1968.
- 17) Scarf, F. L.: Some Comments on the Magnetosphere and Plasma
Environment of Saturn, Space Sciences Department, TRW Systems
Group, 18864-6003-RO-00, 1972.
- 18) Carr, T. D.: Private Communication, 1972.

APPENDIX A: PRODUCTION OF X-RAYS BY BREMSSTRAHLUNG

A single electron of energy E , traversing a thick target of atomic number Z , produces a bremsstrahlung X-ray spectrum given by

$$\frac{dn(\hbar\omega)}{d(\hbar\omega)} = 1.2 \times 10^{-6} Z \left(\frac{E}{\hbar\omega} - 1 \right) \text{ photons/keV}$$

where $dn(\hbar\omega)$ is the number of photons of energy $\hbar\omega \rightarrow \hbar\omega + d(\hbar\omega)$. This result, known as the Kramers formula, is derived in detail in (1); it is valid in the nonrelativistic energy region, and it has been applied successfully to the problem of X-ray production in the earth's auroral zones (22). If the number of electrons with energies between E and $E + dE$ is $\frac{dN}{dE} dE$, the number of photons/keV at an energy $\hbar\omega$ becomes

$$\frac{dn(\hbar\omega)}{d(\hbar\omega)} = 1.2 \times 10^{-6} Z \int_{\hbar\omega}^{\infty} \left(\frac{E}{\hbar\omega} - 1 \right) \frac{dN}{dE} dE$$

An energy spectrum for precipitating electrons which is frequently observed in the earth's auroral zones is

$$\frac{dN}{dE} = C e^{-E/E_0} \text{ electrons/cm}^2 \text{ sec keV} .$$

The parameters C and E_0 (the e-folding energy) are often observed to vary on a time scale of seconds or minutes; however, a typical spectrum can be taken to be

$$\frac{dN}{dE} = 7 \times 10^7 e^{-E/10} \text{ electrons/cm}^2 \text{ sec keV}$$

Although other functional forms can be found which fit the experimental data (22), the exponential spectrum will be used for the following calculations. This gives a photon spectrum at the production region

$$\frac{dn(\hbar\omega)}{d(\hbar\omega)} = 1.20 \times 10^{-6} Z C E_o^2 \frac{e^{-\hbar\omega/E_o}}{\hbar\omega} \text{ X-rays/cm}^2 \text{ sec keV} .$$

To find the X-ray spectrum a distance D away, this expression must be multiplied by $A/4\pi D^2$, where A is the area into which the electrons precipitate. The assumption implicit in this factor is that the X-ray emission is isotropic; this is justified, not by the radiation pattern of the electron, which becomes strongly peaked in the forward direction at higher energies, but rather, by the fact that electron scattering renders the electron flux isotropic in a distance which is small compared to the electron range (1). Thus the X-ray spectrum becomes

$$\frac{dn(\hbar\omega)}{d(\hbar\omega)} = 2.4 \times 10^{-6} C E_o^2 \frac{A}{4\pi D^2} \frac{e^{-\hbar\omega/E_o}}{\hbar\omega} \text{ X-rays/cm}^2 \text{ sec keV} \quad (1A)$$

adopting the value $Z = 2$. Values of C, E_o , and A are derived in Section I.

Another quantity which is of interest is the total number of counts/second which this spectrum will yield in a detector. This is obtained by multiplying the spectrum by the detector area A_d , and the detector efficiency $\epsilon(\hbar\omega)$. Thus the total number of counts/sec in a detector, in the energy window $\hbar\omega_1 \rightarrow \hbar\omega_2$, is

$$n(\hbar\omega_1 \rightarrow \hbar\omega_2) = 2.4 \times 10^{-6} C E_o^2 A \frac{A_d}{4\pi D^2} \int_{\hbar\omega_1}^{\hbar\omega_2} \epsilon(\hbar\omega) \frac{e^{-\hbar\omega/E_o}}{\hbar\omega} d(\hbar\omega) \quad (2A)$$

APPENDIX B:

INSTRUMENT REPORT

PLANETARY X-RAY EXPERIMENT

TABLE OF CONTENTS

	<u>Page</u>
PART I -- INTRODUCTION	1
PART II -- DESIGN STUDY FOR AN X-RAY EXPERIMENT USING SOLID STATE DETECTORS	7
I. THE DETECTOR	8
II. BACKGROUND COUNTING RATES THROUGH THE FORWARD APERTURE	10
A. Diffuse Cosmic X-ray Flux	10
III. LEAKAGE FLUXES	15
A. RTG Gamma Rays	15
B. RTG Neutrons: Direct Effects in Si Detectors	27
C. RTG Neutrons: Indirect Effects Due to Lead Shield	38
D. RTG Neutrons: Indirect Effects in a Cesium Iodide Shield	42
E. Diffuse Cosmic X-ray Leakage	42
F. Cosmic Ray Interactions in the Shield	44
G. Cosmic Ray Interactions in the Spacecraft	44
IV. SUMMARY	46
REFERENCES	49
PART III -- DESIGN STUDY FOR AN X-RAY EXPERIMENT USING A PROPORTIONAL COUNTER	
I. THE DETECTOR	51
II. BACKGROUND COUNTING RATES THROUGH THE FORWARD APERTURE	60
A. Diffuse Cosmic X-ray Flux	60

PART III (CONT.)

III.	LEAKAGE FLUXES	62
A.	RTG Gamma Rays	62
B.	RTG Neutrons: Direct Effects in Proportional Counter	79
C.	RTG Neutrons: Interactions in the Proportional Counter Body	81
D.	RTG Neutrons: Effects Due to Interactions in Lead Shields and Collimators	83
E.	RTG Neutrons: Effects in a CsI Shield	85
F.	Diffuse Cosmic X-ray Flux Leakage	87
G.	Cosmic Ray Interactions in the Proportional Counter	87
H.	Cosmic Ray Interactions in the Spacecraft	88
I.	Summary	90
IV.	CONCLUSION	91
	REFERENCES	92

PART IV -- SUMMARY AND ACKNOWLEDGMENTS	94
--	----

PART I

INTRODUCTION

The basic scientific motivation for an x-ray experiment is to discover the dynamics of the Jovian and Saturnian magnetospheres. Since the Earth's magnetosphere is now reasonably well known, important comparisons can be made for three planetary objects. The x-ray experiment is intended to study particles and plasmas in the magnetospheres and the processes that act on them (e.g., waves, convection). During the encounter with the magnetosphere a profile, essentially at one instant of time, is made by the direct particle counters. There are three major difficulties with such measurements:

1. The spacecraft moves so rapidly that time variations of plasmas, particles and fields cannot be determined except over a narrow range of frequencies.
2. The trajectory cannot explore all regions of interest.
3. It is probably not possible to measure precipitating particle fluxes. These particles carry information about magnetospheric phenomena (waves, auroras, substorms).

The x-ray experiment is intended to remedy these difficulties. The hope is that x-ray fluxes could be detected even months before encounter, then measured from that time until encounter and then for months after the encounter. In that way the pattern of magnetospheric activity could be determined.

The x-ray experiment is one of a group of experiments that can contribute knowledge of planetary magnetospheres. The other experiments are those to measure fields, particles and plasmas while in the magnetosphere; and radio noise emission measured inside as well as outside the magnetosphere. A secondary scientific goal is to make use of the long interplanetary cruise times to study long term variations and transient events in a few cosmic x-ray sources.

Design of a Planetary X-ray Experiment

Some of the design constraints that an outer planetary x-ray experiment must satisfy:

1. Reliable operation for periods up to 10 years.
This requirement demands that gain drifts be very low and that they be corrected in-flight.
2. For very long missions using MHW RTG power sources, the detectors must be insensitive to radiation damage by neutrons and protons. Furthermore, the neutrons and gamma rays from the RTG sources must not contribute very much to the background rate of the detector.
3. The weight should be limited to 3 kg, although more sensitivity may be gained from larger area detectors.
4. The detectors should have good energy ($\sim 30\%$) resolution down to ~ 2 keV photon energy.
5. The angular resolution should be about 0.1° in order to examine satellites of the major planets, and to find the pattern of the x-ray emission on the planet.

The following types of instruments were considered:

1. Grazing incidence focusing optics
 - a. Geiger-Mueller tube detector
 - b. Channeltron detector (for x-ray energies below 1 keV)
 - c. Solid-state detector (small area)
 - d. Proportional counter (small area)
2. Scintillation counter with passive collimator and modulation collimator

3. Solid state detector array with passive and modulation collimators
4. Proportional counter with passive and modulation collimators
 - a. Single wire type
 - b. Multiwire for background rejection

Channeltrons were ruled out because of their short lifetimes (10^{11} counts) and large gain drifts which are difficult to correct for beyond a certain point. The scintillation counter, although feasible from most points of view, does not have the energy resolution of the proportional counter. Also, the weight per square centimeter of sensitive area is more favorable for other detectors. The Si(Li) detector appeared promising at first: its excellent energy resolution might allow surface chemistry experiments on the outer planet satellites without atmospheres.

The grazing incidence x-ray telescope (for example, the hyperboloid-paraboloid type) would allow relatively large x-ray collecting areas to be achieved with small area detectors. In addition, the small field of view would make it possible to do rather detailed mapping of x-ray emission regions. However, at the present state of the art, this type of collimator does not have a high efficiency for x-ray reflection; conventional collimators give equal effective areas for less weight. Therefore, a wire grid modulation collimator, with resolution of about $1/10^0$, appears to be a better choice. In addition, rough collimation, either active or passive, down to a field of about 5^0 square, would be required.

With the choice thus limited to two detectors, and wire grid + active collimator or wire grid + passive collimator, two design studies were undertaken: one for a solid state detector, and one for a proportional counter. These are included as Parts II and III.

It was recognized from the start that the MHW RTGs would be a major problem for the x-ray experiment; therefore, the design studies concentrated on the question of background counting rates, and how to reduce them to an acceptable level with a minimum of weight. At the same time, because the spacecraft design was not finalized, and the MHW RTG radiation levels not known accurately, the emphasis was placed on deriving upper limits to MHW RTG-induced counting rates, and identifying problem areas, rather than obtaining accurate estimates of counting rates. This must await the final design of the spacecraft and RTGs.

The design study for the solid state detector showed that the background counting rate would be quite high, and that a significant portion of it would be caused by RTG neutrons. In addition, radiation damage due to RTG neutrons, as well as radiation belt protons, would be severe with currently produced detectors. Since radiation hardening techniques are being developed, there is at least some hope that the radiation damage problem can be overcome. Therefore, it was decided to proceed experimentally with solid state detectors, to determine whether rise time discrimination could be used to solve the background problem associated with the RTG neutrons. We have tested a Si(Li) detector with two fast rise time (50 ns) preamplifiers; one of these was constructed in our laboratory, and the other is on loan from General Electric, Daytona Beach. Initial results are

not promising: it appears to be impossible to do rise time discrimination in the energy region where the x-ray experiment must work (below 30 keV), due to the very short length of the ionization tracks.

The proportional counter design study is more encouraging; the major problem area was identified as due to RTG gamma rays. Direct interactions in the counter gas, as well as interactions in the counter body giving rise to electrons which deposit energy in the counter are both important effects. However, the use of multiwire counters and/or rise time discrimination can solve these problems; both techniques are currently in use in the energy range of interest. Some passive shielding from the RTGs will be provided by the spacecraft itself; further shielding, either active or passive, will be required at the detector. Since the spacecraft design is still somewhat uncertain, an accurate evaluation of the gamma flux at the detector cannot be made, and the amount of additional shielding needed is not known. On the basis of upper limit estimates, however, the design study shows that a shield weighing about one pound will reduce the background to an acceptable level. This shielding is not required for RTGs as they would be operated on MJS missions. In order to make a more accurate evaluation of active versus passive shields, comparison of geometries, etc. we are currently developing a Monte Carlo program.

Experimentally, two Xenon filled proportional counters are being tested; a third, Krypton counter will be delivered shortly. A delay-line shaping amplifier is being used in conjunction with a pulse shape analyzer to do rise time discrimination. A passive, slat collimator with a built in tungsten wire modulation collimator is

now being designed; this will be constructed in our machine shop and tested in the near future.

PART II

DESIGN STUDY FOR AN X-RAY EXPERIMENT USING SOLID STATE DETECTORS

I. THE DETECTOR

Figure 1 shows the general configuration of the detector assembly used in this study. Four Si(Li) detectors, each .2 cm thick and having .5 cm² area, are used for the 1.5-10 keV range; two Si(Li) detectors, each .2 cm thick and having 5 cm² area, are used for the 10-30 keV range.

These six detectors are placed in the bottom of a square, well-type collimator measuring 10 × 10 × 15 cm, to give approximately a 37° (FWHM) field of view. In the well collimator, above the detectors, is a tungsten wire modulation collimator, with wire spacing approximately equal to wire diameter. (Performance of the modulation collimator, selection of wire diameter and spacing, etc., will be discussed in a later section.) This rather simple geometry has been chosen to simplify the calculations of the background counting rates. Other detector configurations should give approximately the same results, as long as the surface areas and fields of view are approximately the same.

The power source for the Grand Tour spacecraft, a 2200 W(Th) RTG, has been assumed to be 10 feet away from the x-ray experiment, with nothing in between the two. The neutron and gamma radiation levels are thus obtained by $1/r^2$ extrapolation of the levels given by Trainor¹ and Noen and Anno.²

All interactions in the collimator (if it is active) are assumed to give rise to an anticoincidence signal. Since such a signal will contribute to the detector dead time, the background has two effects. First, interactions in the detectors, if they are in the 1.5-30 keV range, contribute to the detector background counting rate; second, shield interactions contribute to the detector dead time. The relative importance

of these two effects is as follows. Suppose that an x-ray source, whose true strength is S counts/sec, must be detected in the presence of a background whose true strength is B counts/sec. The detector dead time is bt , where b is the number of interactions/second producing an anticoincidence pulse, and t is the length of the gate signal for such a pulse. Then in a time interval T , $ST - STbt$ counts are collected from the source, and $BT - BTbt$ from the background. The source will be detected if $ST(1 - bt) \geq 3\sigma_{\text{bkgd}} = 3\sqrt{BT(1 - bt)}$. Thus $T \geq 9B[S^2(1 - bt)]$, and the factor $B/(1 - bt)$ determines the time needed to detect a source.

II. BACKGROUND COUNTING RATES THROUGH FORWARD APERTURE

A. Diffuse Cosmic X-ray Flux

The spectrum of the diffuse flux is:³

$$\begin{aligned}\frac{dN}{dE} &= 10 E^{-1.5} / \text{cm}^2 \text{ sec sr keV}, & 1 < E < 10 \text{ keV} \\ &= 16.8 E^{-1.75} / \text{cm}^2 \text{ sec sr keV}, & 10 < E < 40 \text{ keV} \\ &= 128 E^{-2.3} / \text{cm}^2 \text{ sec sr keV}, & 40 < E < 1000 \text{ keV}\end{aligned}$$

The total fluxes in energy ranges of interest to this experiment are:

$$N(1.5-10) = \int_{1.5}^{10} \frac{dN}{dE} dE = 10 / \text{cm}^2 \text{ sec sr}$$

$$N(10-30) = 2.5 / \text{cm}^2 \text{ sec sr}$$

$$N(>30) = 1.18 / \text{cm}^2 \text{ sec sr}$$

$$N(>200) = .098 / \text{cm}^2 \text{ sec sr}$$

Using geometrical factors of $.052 \text{ cm}^2 \text{ sr}$ for 1.5-10 keV, and $.26 \text{ cm}^2 \text{ sr}$ for 10-30 keV, which assume 100% efficiency for the shield and modulation collimator, the counting rate in the 1.5-10 keV detector is .52 counts/second. In the 1.5-10 keV range, the probability of an interaction in $.2 \text{ cm}$ ($.47 \text{ g/cm}^2$) Si is close to 100%. Above 15 keV, however, the efficiency begins to fall rapidly, and the spectrum must be weighted by $1 - \exp(-\mu_T x)$, where μ_T = total attenuation coefficient, and $x = .47 \text{ g/cm}^2$.

$$\int_{10}^{30} \frac{dN}{dE} (1 - e^{-\mu_T x}) dE \sim 2/\text{cm}^2 \text{ sec sr}$$

Thus the count rate is $2(.26) = .52 \text{ counts/second}$.

The diffuse flux can also contribute to the background count rate by scattering and leaving 1.5-10, or 10-30 keV in the detectors. The graph of Figure 2 shows for $.2 \text{ cm}$ thick Si:

1. The probability of a photon interaction of any kind, $1 - e^{-\mu_T x}$
2. The probability of a Compton interaction leaving 1.5-10 keV,

$$\frac{\sigma_{\text{Compton, 1.5-10}}}{\sigma_{\text{total}}} (1 - e^{-\mu_T x})$$

where the cross sections

$$\sigma_{\text{Compton, 1.5-10}} = \int_{1.5 \text{ keV}}^{10 \text{ keV}} \frac{d\sigma_{\text{Compton}}}{dE} dE$$

σ_{total} = total cross section for interaction of any kind

3. The probability of a Compton interaction leaving 10-30 keV,

$$\frac{\sigma_{\text{Compton, 10-30}}}{\sigma_{\text{total}}} (1 - e^{-\mu_T x})$$

μ_T and σ_T are given by Grodstein⁴; μ_{Compton} is given by Nelms.⁵

Figure 3 shows the diffuse x-ray spectrum, and the product of this spectrum with the three functions of Figure 2. Integrating the bottom two curves of Figure 3, the contribution to the 1.5-10 keV count rate is $7 \times 10^{-2}/\text{cm}^2 \text{ sec sr}$, and the contribution to the 10-30 keV count rate is $2.5 \times 10^{-2}/\text{cm}^2 \text{ sec sr}$. Using geometrical factors of $.208 \text{ cm}^2 \text{ sr}$ and $1.04 \text{ cm}^2 \text{ sr}$ for 1.5-10 and 10-30 respectively (derived by assuming that the modulation collimator is transparent, while the shield is still 100% efficient) the count rates are

.0145 counts/sec, 1.5-10 keV

.0256 counts/sec, 10-30 keV

While these contributions could be reduced by the use of active anticoincidence (since the scattered photons would have a chance of interacting in the bottom of the well and being detected) they are already small enough to be neglected.

Table 1

Background Contributions Due to Diffuse X-rays
(Passive Collimator)

	<u>1.5-10 keV</u>	<u>10-30 keV</u>
Photoelectric interactions	.52 counts/sec	.52 counts/sec
Compton scatter	.0145 counts/sec	.026 counts/sec

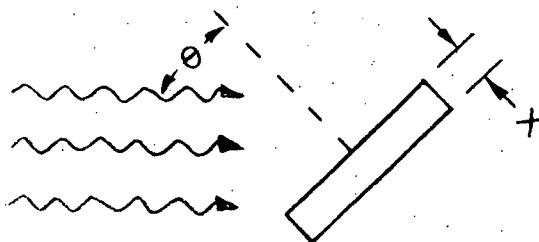
III. LEAKAGE FLUXES

This section deals with fluxes originating outside the field of view of the detectors; i.e., fluxes which leak through the shield.

A. RTG Gamma Rays

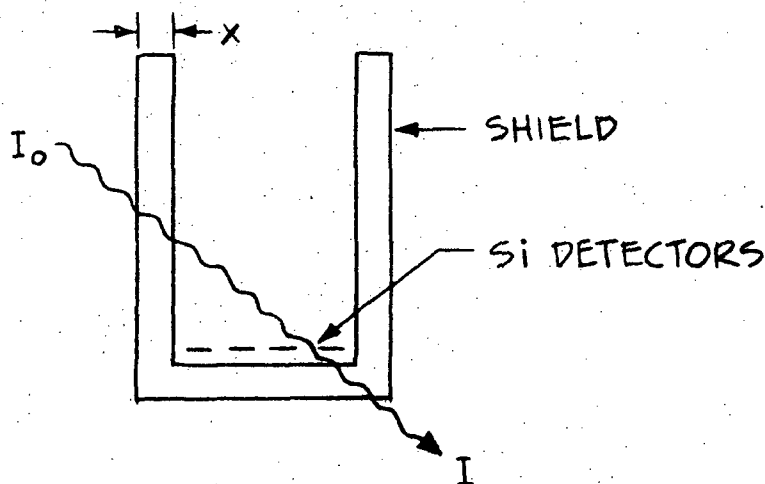
Gamma and neutron fluxes from the RTG are given in Trainor¹ and Noen and Anno²; the gamma spectrum² for 0° and 3 feet is shown in Figure 4 extrapolated by $1/r^2$ to 10 feet.

The background counting rate in the detectors due to this flux will be proportional to $A \cos \theta (1 - e^{-\mu_T x / \cos \theta})$



where A is the detector area, x the thickness, μ_T the total absorption coefficient, and θ is the angle between the incident flux and the detector normal. As long as $(\mu_T x / \cos \theta) \leq .2$, $1 - e^{-\mu_T x / \cos \theta} \sim \mu_T x / \cos \theta$, to 15% or better. Thus the counting rate becomes proportional to $A \mu_T x$, and does not vary with the orientation of the detector. The range of validity of this approximation, as a function of incident flux energy, is shown in Figure 5. Also, since $e^{-x} \geq 1 - x$, $A \mu_T x \geq A \cos \theta (1 - e^{-\mu_T x / \cos \theta})$, so the use of the approximation will give an upper limit to the counting rate even when it is not strictly valid.

Thus Figure 4 also shows the product of the RTG gamma spectrum by the probabilities of Figure 2 and the areas of the 1.5-10 and 10-30 keV detectors. These two graphs show the spectra which would be present in the detectors if there were no collimation at all; the total counting rates are 8 counts/second, 1.5-10, and 49 counts/second, 10-30. The spectra of Figure 4 show that the main contributions are from photons with energies of 10-200 keV. In this energy range, either an active or a passive collimator could be used. An active collimator can attenuate photons either by photoelectric or Compton interactions, and the photon can interact either before or after depositing a count in the Si detector.



Thus the intensity $I = I_0 e^{-2\mu x}$, and the attenuation factor $f_{\text{active}} = 1 - e^{-2\mu x}$.

A passive collimator has only one chance to stop an incoming photon: before it reaches the main detectors, and the interaction must be photoelectric. Thus the attenuation factor

$$f_{\text{passive}} = \frac{\mu_{\text{PE}}}{\mu_{\text{T}}} (1 - e^{-\mu_{\text{T}} x}) \leq \frac{\mu_{\text{PE}}}{\mu_{\text{T}}}$$

where μ_{PE} is the attenuation factor for photoelectric interactions only.

The weight W of a thin wall, well-type shield (Figure 1) is $W = \rho V$, where ρ is the density and V is the volume. If A is the surface area and t is the thickness in cm, $W = \rho A t$. But $\rho t = x$, the thickness in g/cm^2 , so $W = Ax$.

For an active shield,

$$x = -\frac{\ln(1-f)}{2\mu}, \text{ so } W = -\frac{A}{2\mu} \ln(1-f).$$

For a passive shield,

$$x = -\frac{\ln\left(1 - \frac{\mu_{\text{T}}}{\mu_{\text{PE}}} f\right)}{\mu_{\text{T}}}, \text{ so } W = -\frac{A}{\mu_{\text{T}}} \ln\left(1 - \frac{\mu_{\text{T}}}{\mu_{\text{PE}}} f\right)$$

Examples

1. A Silicon shield which actively stops 80% of 200 keV photons:

$$W = -\frac{A}{2 \times .127 \text{ cm}^2/\text{g}} \ln(1-.80) = 6.35 \text{ g/cm}^2 A$$

Thus the shield must be 6.35 g/cm^2 thick; using an area

$A = 700 \text{ cm}^2$, $W = 4400 \text{ gm} = 10 \text{ pounds}$.

2. A CsI shield which actively stops 80% of 200 keV photons:

$$W = -\frac{A}{2 \times .273 \text{ cm}^2/\text{g}} \ln(1-.80) = 2.9A$$

This shield would therefore be 2.9 g/cm^2 thick, and would weigh about 2100 gm, or 4.5 pounds.

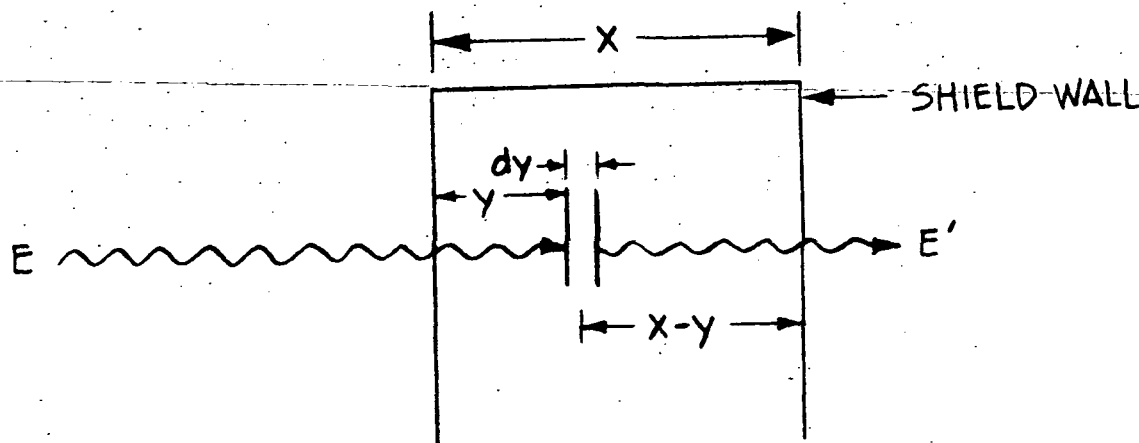
3. A lead shield which passively stops 80% of 200 keV photons:

$$W = - \frac{A}{.942 \text{ cm}^2 \text{ g}} \ln \left(1 - \frac{.942}{.80} \cdot 80 \right) \cong 3A$$

This shield would be about 3 g/cm^2 thick and weigh about 2100 gm, or 4.5 pounds.

The above figures represent upper limits, since the incoming photons were assumed to be normal to the shield. It would appear that the lead shield is preferable, since it does not require any supporting electronics which would add to the weight and complexity of the system. However, the fluorescent x-rays produced in lead and CsI must be compared, since they will contribute to the background counting rate. An upper limit is now derived for this contribution. Assume:

1. That every photoelectric interaction in the shield gives rise to a K x-ray (i.e., ignore the less energetic L, M, etc. x-rays, and the Auger effect).
2. That every fluorescent x-ray leaves the atom in the direction which gives it the shortest escape path through the shield.



The following quantity is now computed:

(Probability of an incoming x-ray of energy E going a distance y with no photoelectric interaction) \times

(Probability of x-ray of energy E photoelectrically interacting in a layer dy thick) \times

(Probability of a fluorescent x-ray of energy E' going a distance $x-y$ with no photoelectric interaction).

For any x-ray, Probability of Interaction + Probability of No Interaction = 1. And Probability of Interaction = Probability of Photoelectron Interaction + Probability of Compton Interaction + Probability of Rayleigh Interaction + (higher order cross terms). Using $P(I)$, $P(NI)$, $P(PE)$, $P(C)$, and $P(R)$ for the above probabilities, and neglecting the cross terms:

$$P(PE) + P(C) + P(R) + P(NI) = 1, \text{ or}$$

$$P(PE) + P(\text{no PE}) = 1, \text{ where}$$

$$\begin{aligned} P(\text{no PE}) &= \text{probability of no photoelectron interaction} \\ &= P(C) + P(R) + P(NI) \end{aligned}$$

$$\text{Since } P(NI) = e^{-\mu y}, P(I) = 1 - e^{-\mu y}, \text{ and}$$

$$P(C) = \frac{\mu_C}{\mu} (1 - e^{-\mu y})$$

$$P(R) = \frac{\mu_R}{\mu} (1 - e^{-\mu y})$$

$$P(PE) = \frac{\mu_{PE}}{\mu} (1 - e^{-\mu y})$$

where $\mu = \mu_{PE} + \mu_C + \mu_R$ is the total interaction coefficient, and μ_{PE} , μ_C , μ_R are the coefficients for photoelectric, Compton, and Rayleigh interactions.

Thus $P(\text{no PE})$ may be written as

$$\begin{aligned} P(\text{no PE}) &= \frac{\mu - \mu_{\text{PE}}}{\mu} (1 - e^{-\mu y}) + e^{-\mu y} \\ &= \frac{\mu_{\text{PE}}}{\mu} e^{-\mu y} + \frac{\mu - \mu_{\text{PE}}}{\mu} \end{aligned}$$

The probability of a photoelectric interaction in a thickness dy is

$$\frac{\mu_{\text{PE}}}{\mu} (1 - e^{-\mu dy}) = \mu_{\text{PE}} dy$$

The probability of no photoelectric interaction in a distance $x-y$, for an energy E' (coefficients μ'_i) is

$$\frac{\mu'_{\text{PE}}}{\mu'} e^{-\mu'(x-y)} + \frac{\mu' - \mu'_{\text{PE}}}{\mu'}$$

Multiplying the above three probabilities together, and integrating over y values from x to 0, we get for the probability that an incoming photon of energy E produces a fluorescent photon of energy E' which escapes,

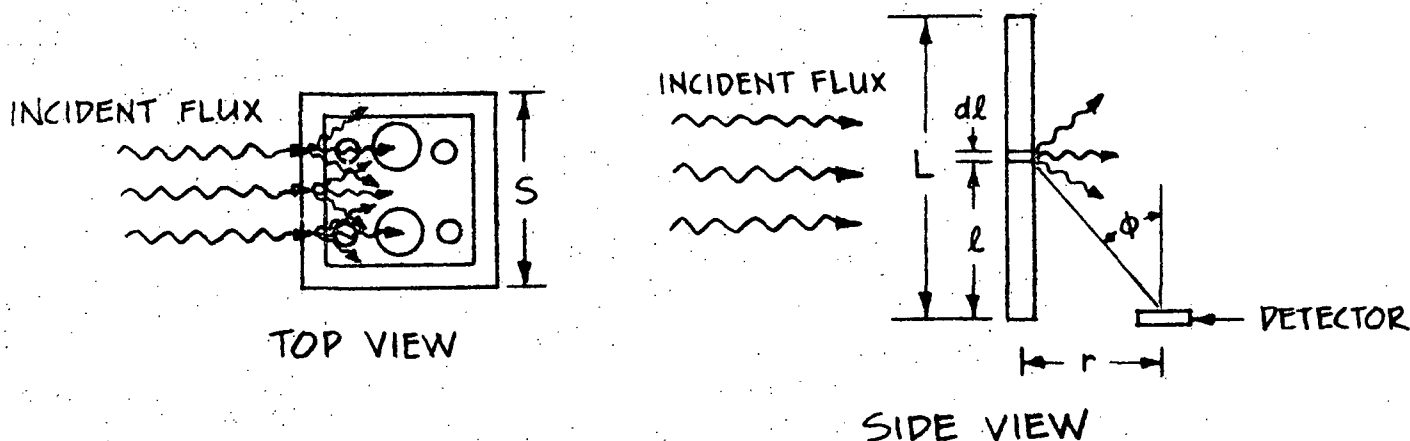
$$\begin{aligned} \mu_{\text{PE}} \left\{ \frac{\mu_{\text{PE}}}{\mu} \frac{\mu'_{\text{PE}}}{\mu'} \frac{e^{-\mu x} - e^{-\mu' x}}{\mu' - \mu} + \frac{\mu_{\text{PE}}}{\mu} \frac{\mu' - \mu'_{\text{PE}}}{\mu'} (1 - e^{-\mu x}) + \right. \\ \left. \frac{\mu - \mu_{\text{PE}}}{\mu} \frac{\mu' - \mu'_{\text{PE}}}{\mu'} x + \frac{\mu - \mu_{\text{PE}}}{\mu} \frac{\mu'_{\text{PE}}}{\mu'} \frac{1 - e^{-\mu' x}}{\mu'} \right\} \end{aligned}$$

For lead, take $E = 200 \text{ keV}$, $E' = 80 \text{ keV}$, $x = 3 \text{ g/cm}^2$, $\mu_{\text{PE}} = .80 \text{ cm}^2/\text{g}$, $\mu = .94 \text{ cm}^2/\text{g}$, $\mu'_{\text{PE}} = 1.29 \text{ cm}^2/\text{g}$, $\mu' = 1.66 \text{ cm}^2/\text{g}$. The probability then becomes .32.

For CsI, take $E = 200$ keV, $E' = 30$ keV; $x = 2.9$ g/cm², $\mu_{PE} = .250$ cm²/g, $\mu = .272$, $\mu'_{PE} = 6.33$, $\mu' = 6.34$. The probability for CsI becomes .02.

How many of these escaping photons interact in the detectors?

To get an upper limit to this number, assume that the escaping photons are distributed isotropically, and let n be the number which escape per cm² per second.



A thin strip sdl emits $nsdl$ photons/second, and the flux at a distance $(l^2 + r^2)^{\frac{1}{2}}$ from this strip is $nsdl/4\pi(l^2 + r^2)$. The detector (area A) presents an effective area $A \cos\phi$ to this flux, and the probability that a photon will interact in the detector is $1 - e^{-\mu x / \cos\phi}$. Thus as an upper limit to the contribution from the thin strip, we have $\frac{nsdl}{4\pi(l^2 + r^2)} A \mu x$. Integrating over l values from 0 to L , this becomes

$$\frac{nsA\mu x}{4\pi} \frac{1}{r} \tan^{-1} \frac{L}{r}$$

Typical values are $r = 5$ cm, $L = 15$ cm and $s = 10$ cm, so we get $.2n A \mu x$.

From Figure 4, the incident flux of 200 keV photons is $1.5 \times 10^2 / \text{cm}^2 \text{ sec}$. Thus for a lead shield, $n = (.32)(1.5 \times 10^2) = 48 / \text{cm}^2 \text{ sec}$. From Figure 2, the contribution to the low energy detectors is $(48)(2)(.2)(3.5 \times 10^{-2}) = .67 \text{ counts/sec}$ and the contribution to the high energy detectors is $(48)(10)(.2)(3 \times 10^{-2}) = 2.9 \text{ counts/sec}$.

For the CsI shield, $n = (.02)(1.5 \times 10^2) = 3 / \text{cm}^2 \text{ sec}$ and from Figure 2 the low energy contribution is $(3)(2)(.2)(3 \times 10^{-2}) = .036 \text{ counts/sec}$. Since a 30 keV photon can leave at most several keV to an electron in a Compton interaction, the contribution to the high energy detectors will be through photoelectric interactions only. From Figure 2, the probability of an interaction of any kind is 50% at 30 keV; the ratio of photoelectric to total cross-section is $1.17/1.44$.⁴ Thus the contribution to the high energy detectors is $(3)(10)(.2)(.5)(1.17/1.44) = 2.4 \text{ counts/sec}$. However, most of the CsI fluorescent x-rays will be gated out by means of the initial interaction in the shield.

Since 80% of the 200 keV photons interact in the shield, the contribution to the dead time is $(.8)(1.5 \times 10^2)(1.5 \times 10^2 \text{ cm}^2) = 1.8 \times 10^4 \text{ counts/sec}$.

The two shields considered above both stop 80% of the incident 200 keV photons; to complete the comparison, the leakage at other energies must be computed. Thus the graph of Figure 6 shows the probability of no photoelectric interaction in 3 g/cm^2 of lead, as derived on page 14, and the graph of Figure 7 shows the probability of no interaction at all in $2 \times 2.9 \text{ g/cm}^2$ of CsI, as defined on page 21. Finally, the product of these probabilities with the 1.5-10 keV graph of Figure 4 gives the flux of photons which leaks through the shield and

scatters in the low energy detector, leaving 1.5-10 keV. This is shown in Figure 8, where a direct comparison of the active and passive shield counting rates (excluding the effect of fluorescent x-rays) may be made. Since the contribution from 100-200 keV photons is about an order of magnitude larger than any other contribution, and the shields have identical stopping powers in the 100-200 keV range, the difference between the two is negligible. The comparison is summarized in Table II.

Table II

	<u>RTG Photon Count Rates</u>				
	Passive Shield (keV)		Active Shield (keV)		
	<u>1.5-10</u>	<u>10-30</u>	<u>1.5-10</u>	<u>10-30</u>	<u>Dead Time</u>
Leakage	1.6 c/s	9 c/s	1.6 c/s	9 c/s	1.8×10^4 c/s
Fluorescence	.67 c/s	2.9 c/s	0	0	

B. RTG Neutrons: Direct Effects in Si Detectors

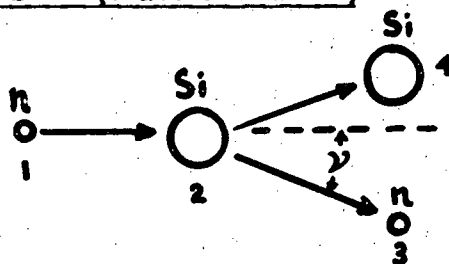
The RTG neutron spectrum of Figure 9 was obtained by $1/r^2$ extrapolation to 10 feet of the spectrum given in Trainor.¹ It will be shown in section C that both the active and passive shields are almost transparent to neutrons; thus the entire spectrum of Figure 9 may be considered to be incident on the Si detectors. The possible interactions of neutrons with Si are:

1. $\text{Si}^{28} (n, n) \text{Si}^{28}$ (elastic scatter)
2. $\text{Si}^{28} (n, n') \text{Si}^{28*}$ (inelastic scatter)
3. $\text{Si}^{28} (n, p) \text{Al}^{28}$; threshold energy 3.86 MeV.⁶
 $\text{Al}^{28} \rightarrow \beta^- + \text{Si}^{28}$, $T_{1/2} = 2.3$ minutes.

4. $\text{Si}^{28} (n, \alpha) \text{Mg}^{25}$; threshold energy 2.66 MeV⁶

Figure 10 shows the cross-sections for these interactions as a function of energy⁷ and Figure 11 shows the probabilities of these interactions in .47 g/cm² Si (E.g., the probability of an elastic scatter is $(\sigma_{\text{elastic scatter}}/\sigma)(1 - e^{-\sigma x})$ where x is the thickness of the material, σ is the total cross-section for an interaction of any kind, and $\sigma_{\text{elastic scatter}}$ is the elastic scattering cross-section.)

1. $\text{Si}^{28} (n, n) \text{Si}^{28}$ (elastic scatter)



Energy is left in the detector by the recoiling silicon nucleus. Thus the energy E_4 must be found as a function of the neutron scattering angle v , and the form of the differential cross-section must be known, in order to compute the probability of an incident neutron leaving a countable energy in the detector. In particular, the values of v must be found for which $.0015 \text{ MeV} \leq E_4 \leq .010 \text{ MeV}$ or equivalently, $E_1 - .010 \text{ MeV} \leq E_3 \leq E_1 - .0015 \text{ MeV}$ (a low energy count) and $.010 \leq E_4 \leq .030$, or equivalently, $E_1 - .03 \leq E_3 \leq E_1 - .01$ (a high energy count). The energies and angles are related by (Evans⁸)

$$\sqrt{E_3} = \sqrt{E_1} \left\{ \frac{\cos v}{29} + \sqrt{\frac{\cos^2 v}{29^2} + \frac{27}{29}} \right\}.$$

Differential cross-section data are apparently not available for ^{14}Si ; on the assumption that the difference between one element and its neighbor will not be very great, the data for ^{13}Al were used.⁷

The results are summarized in Table III. The pulse height defect, due to nuclear (non-ionizing) collisions, will increase these numbers slightly.⁶

2. $\text{Si}^{28} (n, n') \text{Si}^{28*}$ (inelastic scatter)

From Figure 11, the probability is $\leq 2 \times 10^{-2}$, so the total number of interactions (using a total incident flux of $8.4 \times 10^2/\text{cm}^2 \text{ sec}$) is $\leq 17 \text{ cm}^2 \text{ sec}$. The first excited level in Si^{28} is 1.78 MeV above ground.⁹ Thus from Figure 2, the probability of leaving a count in the low energy detector is at most $\sim 10^{-4}$, and for the high energy detector, $\sim 2 \times 10^{-4}$. The contributions to the counting rates are therefore

$$(17)(10^{-4})(2) = .0034 \text{ counts/sec, } 1.5\text{-}10 \text{ keV}$$

$$(17)(2 \times 10^{-4})(10) = .034 \text{ counts/sec, } 10\text{-}30 \text{ keV}$$

3. $\text{Si}^{28} (n, p) \text{Al}^{28}$; $\text{Al}^{28} \rightarrow \beta^- + \text{Si}^{28}$, $T_{1/2} = 2.3 \text{ min}$

From Figure 11, the probability of this reaction is $\leq 6 \times 10^{-3}$, and the threshold is 3.86 MeV. For incident neutron energies in the range $3.86 \leq E \leq 3.96$, the proton is left with $E \leq 30 \text{ keV}$.⁸ From Figure 9, a rough estimate of the number of incident neutrons in this energy range is $\sim 3/\text{cm}^2 \text{ sec}$. Thus as upper limits to the count rates from this reaction we have

$$(3)(6 \times 10^{-3})(2) = .036 \text{ counts/sec, } 1.5\text{-}10 \text{ keV}$$

$$(3)(6 \times 10^{-3})(10) = .18 \text{ counts/sec, } 10\text{-}30 \text{ keV}$$

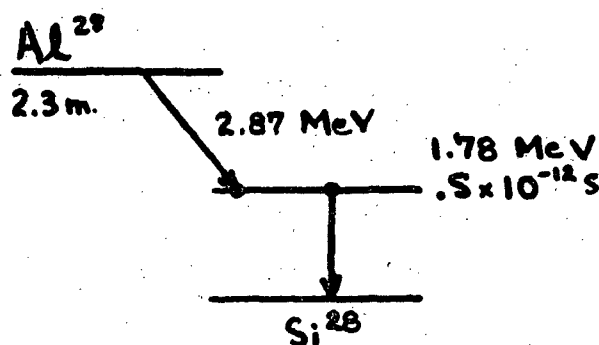
The Al^{28} nucleus may be formed in an excited state; the first energy level is 31 keV above ground and up to excitation energies of 7.7 MeV, de-excitation is by gamma emission.⁹ The 31 keV level has a lifetime of about $2 \times 10^{-9} \text{ sec}$; angular momenta for higher levels are uncertain, but de-excitation probably by dipole transition, so other

Table III

Neutron Energy MeV	Probability of (n,n) Reaction (Figure 11)	Scattering Angle for Leaving		Fraction of Total Cross-section for Leaving		Probability of Leaving		Contribution to	
		1.5-10 keV	10-30 keV	1.5-10 keV	10-30 keV	1.5-10 keV	10-30 keV	1.5-10 keV Detector (Figure 9)	10-30 keV Detector (Figure 9)
1	3×10^{-2}	0-30°	30-55°	$\frac{27}{111}$	$\frac{30}{111}$	$.73 \times 10^{-2}$	$.81 \times 10^{-2}$	4.6 c/s	25 c/s
1.5	1.5×10^{-2}	0-25°	25-44°	$\frac{21}{111}$	$\frac{25}{111}$	$.28 \times 10^{-2}$	$.34 \times 10^{-2}$	1.8 c/s	10 c/s
2.5	1.1×10^{-2}	0-18°	18-33°	$\frac{14}{111}$	$\frac{16}{111}$	$.14 \times 10^{-2}$	$.16 \times 10^{-2}$	6.2×10^{-1} c/s	3.5 c/s
3.5	1.1×10^{-2}	0-15°	15-28°	$\frac{10}{111}$	$\frac{15}{111}$	$.10 \times 10^{-2}$	$.15 \times 10^{-2}$	6.5×10^{-2} c/s	5.8×10^{-1} c/s
TOTAL								7.1 c/s	39 c/s

lifetimes are of this order of magnitude. Thus radiative de-excitation of the Al^{28} nucleus will be coincident with the energy loss of the proton, and no extra counts will result.

The beta emission of Al^{28} is followed by a radiative de-excitation of the Si^{28} nucleus. These events may deposit counts in the detectors since they occur several minutes after the (n,p) reaction.



The end point of the beta spectrum is 2.87 MeV; thus a beta can deposit a count either by being ejected with an energy less than 30 keV, or by being ejected with a higher energy near the surface of the detector, and losing less than 30 keV before it escapes. The beta spectrum should look like the one given by Evans⁸ in his Figure 1.4. Thus a very rough estimate of the fraction of betas created with an energy less than 30 keV is $\sim 2 \times 10^{-3}$. From Figure 9, the number of incident neutrons above the threshold energy is approximately $30 \text{ cm}^2 \text{ sec}$; since the probability of a (n,p) reaction is about 6×10^{-3} , the number of betas created with $E \leq 30 \text{ keV}$ is $(30)(6 \times 10^{-3})(2 \times 10^{-3}) = 3.6 \times 10^{-4} / \text{cm}^2 \text{ sec}$.

For betas with energies around 2 MeV, $dE/dx \cong .4 \text{ keV/micron}^{10}$ in silicon; thus a beta would have to traverse only 3-70 microns to lose 1.5-30 keV. The probability of a (n,p) reaction in the top or bottom 70 microns is (Figure 10)

$$2 \times \frac{.4 \text{ barns}}{3 \text{ barns}} \left(1 - e^{-6.4 \times 10^{-2} \text{ cm}^2/\text{g} \times 1.65 \times 10^{-2} \text{ g/cm}^2} \right) \\ \cong 2.8 \times 10^{-4}$$

Using $30/\text{cm}^2 \text{ sec}$ neutrons above threshold energy, the number of interactions producing a count is roughly $84 \times 10^{-4}/\text{cm}^2 \text{ sec}$.

An interaction of the 1.78 gamma, since it is coincident with the beta, would simply add to the energy deposited by the beta. Thus these events will be neglected. The total number of interactions producing counts is then $88 \times 10^{-4}/\text{cm}^2 \text{ sec}$ and the contributions are

.018 counts/sec, 1.5-10 keV

.088 counts/sec, 10-30 keV

from the decay of the Al^{28} nucleus. Adding these to the (n,p) contributions on page 24, the totals are

.054 counts/sec, 1.5-10 keV

.27 counts/sec, 10-30 keV

4. $\text{Si}^{28} (n, \alpha) \text{Mg}^{25}$

The probability of this reaction is $\sim 10^{-3}$ (Figure 11), and the threshold is 2.66 MeV. Using an incident flux of $210/\text{cm}^2 \text{ sec}$, $21/\text{cm}^2 \text{ sec}$ reactions take place. Mg^{25} is a stable nucleus; up to an energy of about 7 MeV above ground, de-excitation is by gamma emission, and the first excited state is .6 MeV above ground.⁹ Lifetimes are of

the order of 10^{-9} seconds, so the gamma energy loss is coincident with the alpha.

As above, the alpha can leave a countable energy either by being emitted with an energy of less than 30 keV, or by being emitted with a higher energy near the surface of the detector.

For incident neutron energies $2.65 \leq E \leq 2.9$ MeV, the alpha is emitted with less than ~ 30 keV. From Figure 9, roughly $55/\text{cm}^2 \text{ sec}$ neutrons are incident with these energies, so the contribution from this type of interaction is $.055/\text{cm}^2 \text{ sec}$.

At higher energies, $dE/dx = 200$ keV/micron for alphas;¹⁰ to lose 30 keV, an alpha must traverse only 7 microns, and the probability of a (n, α) reaction in the top or bottom 7 microns is approximately

$$2 \times \frac{.1 \text{ barn}}{3 \text{ barns}} \left(1 - e^{-6.4 \times 10^{-2} \text{ cm}^2/\text{g} \times 1.65 \times 10^{-3} \text{ g/cm}^2} \right) \\ \cong 7 \times 10^{-5}$$

Using an incident flux of $210/\text{cm}^2 \text{ sec}$ above threshold, the contribution is $.015/\text{cm}^2 \text{ sec}$. Thus the total number of counts/second is

$$(.07)(2) = .14 \text{ counts/sec, } 1.5\text{-}10 \text{ keV}$$

$$(.07)(10) = .7 \text{ counts/sec, } 10\text{-}30 \text{ keV}$$

Table IV summarizes the effects of neutrons in silicon.

Table IV

<u>Interaction</u>	<u>Count Rates Due to Interaction</u>	
	<u>1.5-10 keV</u>	<u>10-30 keV</u>
(n, n)	7.1 c/s	39 c/s
(n, n')	.0034 c/s	.034 c/s
(n, p)	.054 c/s	.27 c/s
(n, α)	.14 c/s	.7 c/s

C. RTG Neutrons: Indirect Effects Due to Lead Shield

The following neutron reactions can occur in the lead shield:

1. $\text{Pb}^{207} (n, n) \text{Pb}^{207}$ (elastic scatter)
2. $\text{Pb}^{207} (n, n') \text{Pb}^{207*}$ (inelastic scatter)
3. $\text{Pb}^{207} (n, \gamma) \text{Pb}^{208}$

The cross-sections for these reactions are shown in Figure 12, and the probabilities for 3 g/cm² of lead are shown in Figure 13.

1. $\text{Pb}^{207} (n, n) \text{Pb}^{207}$ (elastic scatter)

This reaction has the effect of scattering neutrons, not headed for the detectors initially, into the detectors. Using the formula on page 23, and noting that the transparency of the lead shield to neutrons means that neutrons have two chances to scatter, $.4n$ neutrons/cm² sec head for the detectors, where n is the number/cm² sec which elastically scatter. Since 8.4×10^2 /cm² sec are incident, and the probability of an elastic scatter is $\leq 4.5 \times 10^{-2}$, $15/\text{cm}^2$ sec will be scattered into the detectors. Referring to Table III, the maximum contributions are:

$$(15)(2)(.73 \times 10^{-2}) = .22 \text{ c/s, } 1.5\text{-}10 \text{ keV}$$

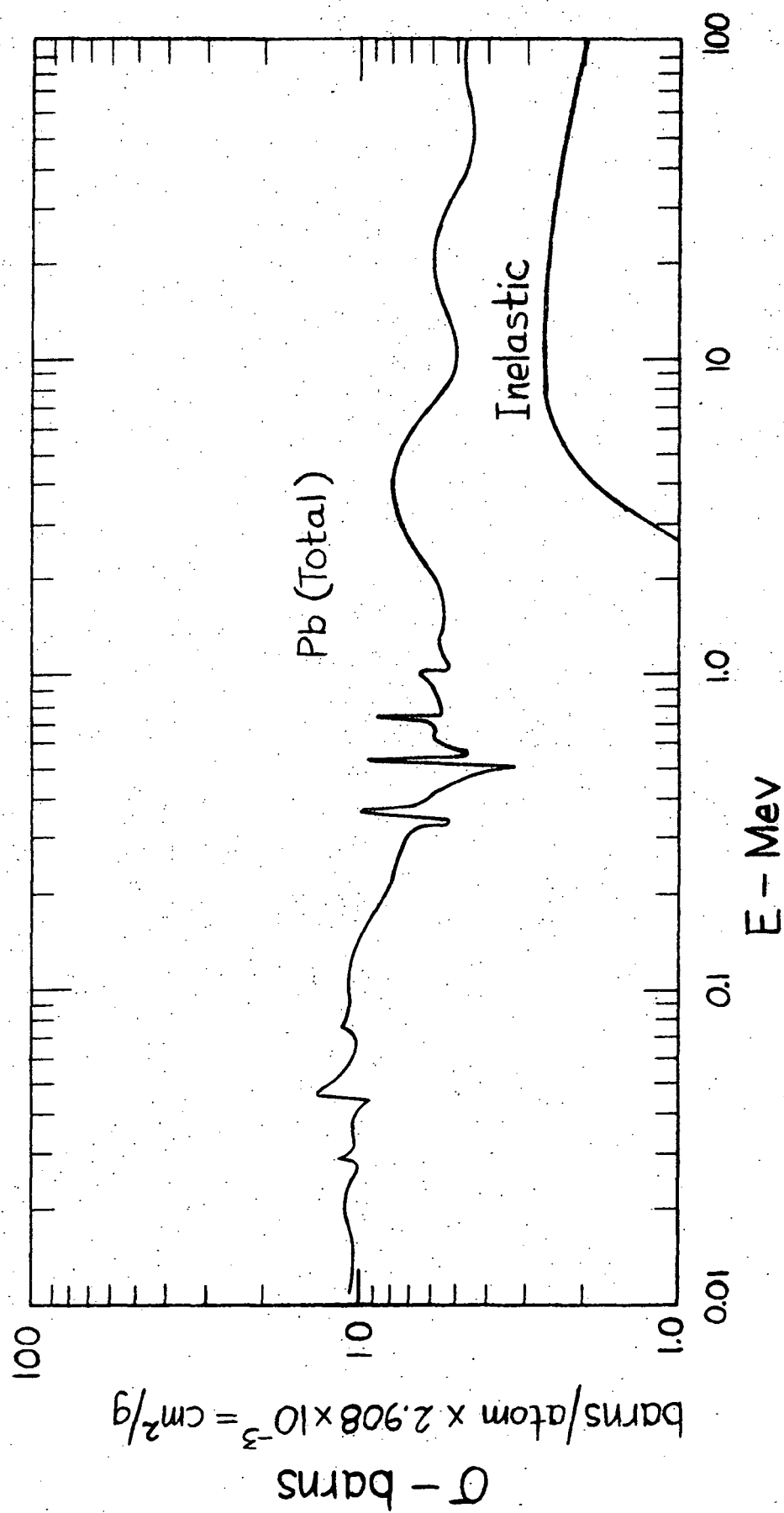
$$(15)(10)(.81 \times 10^{-2}) = 1.2 \text{ c/s, } 10\text{-}30 \text{ keV}$$

2. $\text{Pb}^{207} (n, n') \text{Pb}^{207*}$ (inelastic scatter)

Since the probability of an inelastic scatter is at most about one-half the probability of an elastic scatter, the contributions from scattered neutrons will be about one-half of those given above:

$$.11 \text{ c/s, } 1.5\text{-}10 \text{ keV}$$

$$.6 \text{ c/s, } 10\text{-}30 \text{ keV}$$



Cross Sections for Neutron Interactions in Pb^{207} (From (7))

For excitation energies up to about 6.7 MeV, the Pb^{207} nucleus de-excites by gamma emission. From Figure 13, the number of inelastic scatters is $\leq (8.4 \times 10^{+2})(2.5 \times 10^{-2}) = 21/\text{cm}^2 \text{ sec}$. The first excited state is .57 MeV above ground, so from Figure 2, the contributions are:

$$(.4)(21)(2)(8.5 \times 10^{-4}) = .014 \text{ c/s, } 1.5\text{-}10 \text{ keV}$$

$$(.4)(21)(10)(2 \times 10^{-3}) = .168 \text{ c/s, } 10\text{-}30 \text{ keV}$$

Thus the total contributions due to neutrons and gammas from this interaction are:

$$.12 \text{ c/s, } 1.5\text{-}10$$

$$.23 \text{ c/s, } 10\text{-}30$$

3. $\text{Pb}^{207} (n, \gamma) \text{Pb}^{208}$

The Q value for this reaction, using the mass defect values given by Leighton,¹ is $37.79 + 8.36 - 38.77 = -7.4 \text{ MeV}$. De-excitation of the stable Pb^{208} nucleus follows by gamma emission direct to ground in $\geq 90\%$ of the cases.⁹ As there are evidently no neutrons with energies above 5 MeV, this reaction can be neglected.

Table V summarizes the effects of RTG neutrons due to a lead shield.

Table V

Effects of RTG Neutron Interactions in a Lead Shield

<u>Interaction</u>	<u>Counting Rates</u>	
	<u>1.5-10 keV</u>	<u>10-30 keV</u>
(n, n)	.22 c/s	1.2 c/s
(n, n')	.12 c/s	.23 c/s

D. RTG Neutrons: Indirect Effects in a CsI Shield

The following interactions can occur with the I^{127} nucleus:

1. $I^{127} (n, n) I^{127}$ (elastic scatter)
2. $I^{127} (n, n') I^{127*}$ (inelastic scatter)
3. $I^{127} (n, \gamma) I^{128}$; $I^{128} \rightarrow \beta^- + Xe^{128}$ ($T_{1/2} = 25$ minutes)

(Beta spectrum end point is 2.12 MeV)

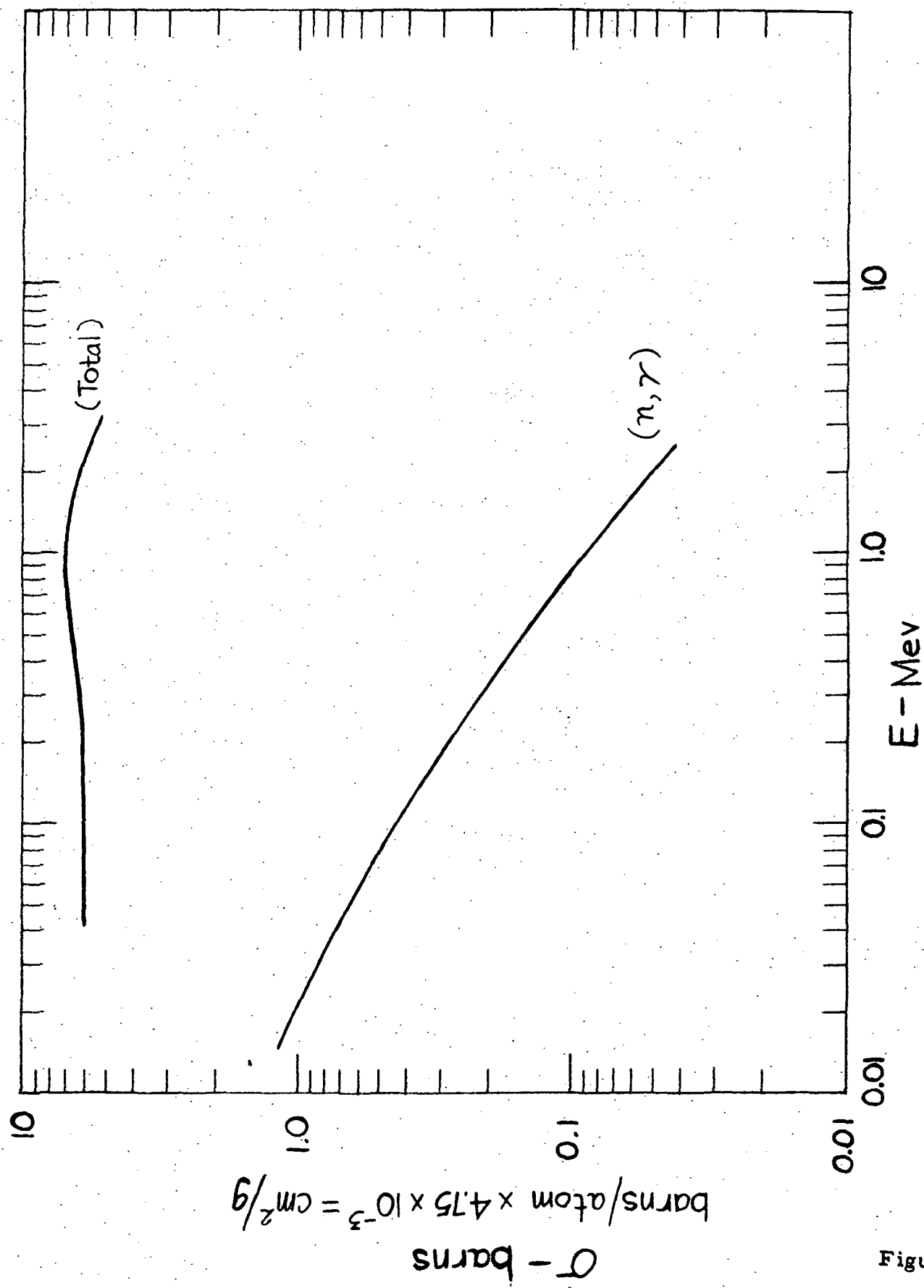
The Iodine cross-sections are shown in Figure 14, reproduced from Hughes;⁷ Cs cross-sections are evidently not available. Since the total iodine cross-section is approximately 6 barns/atom = $.0285 \text{ cm}^2/\text{g}$, the shield is almost transparent to neutrons. Noting that this transparency gives most neutrons two chances to interact, and each passage through the shield (2.9 g/cm^2 thick) involves approximately 1.45 g/cm^2 . Iodine, the fraction which interacts is $1 - e^{-2.9 \times .0285} \cong .0825$. Since the recoiling Iodine nucleus would cause an anticoincidence signal for most of the above reactions, interactions in the active shield would cause no extra counts in the detectors. However, the contribution to the dead time would be $(.0825)(8.4 \times 10^2/\text{cm}^2 \text{ sec})(150 \text{ cm}^2) = 10^4 \text{ c/s}$.

E. Diffuse Cosmic X-ray Leakage

An upper limit to this leakage flux can be had by considering the total number of diffuse x-rays with energies greater than 200 keV since the shield becomes quite transparent at higher energies. From page 10, this is approximately $10^{-1}/\text{cm}^2 \text{ sec sr}$. Using Figure 2, the number of interactions is

$$\leq (10^{-1})(4\pi)(2)(3 \times 10^{-3}) = .0024 \text{ c/s, } 1.5\text{-}10 \text{ keV}$$

$$\leq (10^{-1})(4\pi)(10)(1.5 \times 10^{-2}) = .06 \text{ c/s, } 10\text{-}30 \text{ keV}$$



Cross Sections for Neutrons in Iodine (From (7))

From page 10, the number of diffuse x-rays $10 < E < 200$ is $3.6/\text{cm}^2 \text{ sec sr}$. Almost all of these would interact in an active shield, giving a dead time contribution of 1.35×10^4 counts/second.

F. Cosmic Ray Interactions in the Shield

Using a cross-section of $.0125 \text{ cm}^2/\text{g}$ for cosmic rays, a 3 g/cm^2 shield will cause a fraction $(1 - e^{-2 \times 3 \times .0125}) = 7.5 \times 10^{-2}$ of incident cosmic rays to interact. Over $2\pi \text{ sr}$, there are approximately $6.28 \text{ cosmic rays/cm}^2 \text{ sec}$ and $.47 \text{ interactions/cm}^2 \text{ sec}$. Using the argument of page 23 and noting that there are four walls of the shield producing gamma rays, $(.8)(.47) = .38 \text{ gammas/cm}^2 \text{ sec}$ are directed towards the detectors, if every cosmic ray interaction produces a gamma ray. Using the maximum probabilities of Figure 2 to obtain an upper limit, we have

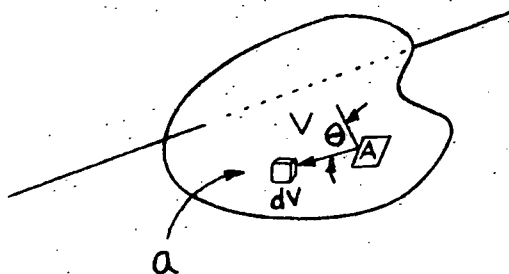
$$(.38)(2)(6 \times 10^{-2}) = 4.5 \times 10^{-2} \text{ c/s, } 1.5\text{-}10 \text{ keV}$$

$$(.38)(10)(3 \times 10^{-2}) = .11 \text{ c/s, } 10\text{-}30 \text{ keV}$$

In an active shield, $(.47)(600 \text{ cm}^2) = 2.8 \times 10^2 \text{ interactions/sec}$ would occur.

G. Cosmic Ray Interactions in the Spacecraft

If N is the flux of cosmic rays (per $\text{cm}^2 \text{ sec sr}$), $N\pi a$ cosmic rays/sec will be incident on the area a bounding a volume V .



If the volume V has a mass W , a typical path through the volume has a thickness $W/a \text{ g/cm}^2$. Using a mean free path of 80 g/cm^2 for cosmic rays, the probability of an interaction is $1 - e^{-W/80a}$. Rough estimates

give $W = 6.5 \times 10^5 \text{ g}$ and $a = 6 \times 10^4 \text{ cm}^2$ for the Grand Tour spacecraft, so $W/a = 11 \text{ g/cm}^2$, and the probability is approximately $W/80a$ in this case. Thus the number of interactions per second is $N\pi a W/80a = N\pi W/80$. Assuming uniform production of gammas throughout the volume, and assuming that each interaction produces a gamma ray, then a small volume dV produces $\frac{N\pi W}{80} \frac{dV}{V} \gamma/\text{sec}$. The flux at a detector a distance r from dV is $\frac{N\pi W}{80} \frac{dV}{V} \frac{1}{4\pi r^2} \gamma/\text{cm}^2 \text{ sec}$. A detector of area A , whose normal makes an angle θ with r , will intercept

$$\frac{N\pi W}{80} \frac{dV}{V} \frac{1}{4\pi r^2} A \left(1 - e^{-\mu x / \cos \theta}\right) \cos \theta \cong \frac{N\pi W}{80} \frac{dV}{V} \frac{A\mu x}{4\pi r^2} \gamma/\text{sec}.$$

Thus the number of counts/second due to the entire volume is

$$\frac{N\pi W}{80} \frac{1}{V} \frac{A\mu x}{4\pi} \int \frac{dV}{r^2}$$

Evaluation of this integral for simple geometries (spheres and cylinders) shows that it is of the order $4\pi r$, where r is a characteristic dimension of the object. Taking the case of a sphere, with the detector at the center, there will be

$$\frac{N\pi W}{80} \frac{1}{\frac{4}{3}\pi r^3} \frac{A\mu x}{4\pi} = \frac{N\pi W}{80} \frac{3}{4\pi r^2} A\mu x = \frac{N\pi}{80} \left(\frac{W}{a}\right)^3 A\mu x$$

Using $N = 1$, $W/a = 10 \text{ g/cm}^2$, this becomes $1.2 A\mu x$ counts/sec.

Taking the maximum probabilities from Figure 2, we get

$$(1.2)(2)(6 \times 10^{-2}) = .14 \text{ c/s, } 1.5\text{-}10 \text{ keV}$$

$$(1.2)(10)(3 \times 10^{-2}) = .36 \text{ c/s, } 10\text{-}30 \text{ keV}$$

IV. SUMMARY

The emphasis has been on the derivation of upper limits; a number of factors could reduce the counting rates. Among them are (1) the presence of matter between the RTGs and the detectors (for example, the propulsion bay might cast a "shadow" on the science end of the spacecraft); and (2) the presence of a housing around the science portion of the spacecraft. While these might not do much for the neutron induced background, they would certainly reduce the gamma background. In addition, a housing might reduce the necessary shield thickness.

To complete the comparison between the active and passive shields, Table VI summarizes the counting rates from all sources for an active and for a passive shield. To compute the factor $B/(1-bd)$, a dead time gate length must be assumed. Under normal circumstances, a reasonable assumption might be that a 30 microsecond gate is generated whenever an interaction occurs in the shield. In the present case, however, the shield is counting a large number of interactions due to the RTGs, and only a small fraction of these interactions results in a count occurring in the main detectors. Thus it might be feasible to send the main detector pulses through a delay line, meanwhile analyzing the main detector and shield pulses (perhaps by means of a peak detector) for coincidence to within a microsecond or so, and generate a 30 microsecond gate only for true coincidence between the shield and the main detector. In this way, the amount of spurious dead time could be reduced to almost zero. As Table VI shows, the number of counts per second in the shield is 4.1×10^4 , which is sufficient to cause 100% dead time with a 30 microsecond gate length.

Table VI

Source	Passive Collimator (counts/second)		Active Collimator (counts/second)		Dead Time
	1.5-10 keV	10-30 keV	1.5-10 keV	10-30 keV	
Cosmic X-rays (Forward Aperture)	.53	.55	.52	.52	--
RTG Gammas	2.3	12	1.6	9	1.8×10^4
RTG Neutrons (Direct Effects)	7.3	40	7.3	40	--
RTG Neutrons (Indirect Effects)	.34	1.5	0	0	10^4
Cosmic X-ray Leakage	.0024	.06	~0	~0	1.3×10^4
Cosmic Ray Interactions in Shield	.045	.11	0	0	2.8×10^2
Cosmic Ray Interactions in Spacecraft	.14	.36	~.14	~.36	~0
TOTALS	10.65	54.58	9.56	49.88	4.1×10^4
TOTALS WITHOUT NEUTRON CONTRIBUTIONS	3.01	13.08	2.26	9.88	

The total background counting rates are computed with all interactions included, and with all interactions except neutron interactions included; since neutron interactions are responsible for most of the background counts, some sort of pulse shape discrimination should be investigated to reject this contribution.

REFERENCES

1. 701-101 TOPS-3-300; a section of this report was included in a private communication to K.A. Anderson from J.H. Trainor, dated April 10, 1968
2. Noen, E.L. and G.H. Anno, Radiation Analysis of the Helipak Fuel Source Design, private communication to K.A. Anderson, October 21, 1970
3. Silk, J., Diffuse Cosmic X- and Gamma Radiation: The Isotropic Component, Space Sci. Rev., 11, 671, 1970
4. Grodstein, G.W., X-ray Attenuation Coefficients from 10 keV to 100 MeV, NBS Circular 583, 1957
5. Nelms, A.T., Graphs of the Compton Energy-Angle Relationship and the Klein-Nishina Formula from 10 keV to 500 MeV, NBS Circular 542, 1953
6. Bertolini, G., Semiconductor Detectors, North-Holland Publ. Co., Amsterdam, p. 430, 1968
7. Hughes, D.J., Neutron Cross Sections, Brookhaven National Laboratory Report BNL 325, 1955 and 1958 (U.S. Government Printing Office, Washington, D.C.)
8. Evans, R.D., The Atomic Nucleus, McGraw-Hill Book Co., New York, 1955
9. Landolt-Bornstein, H.H., Numerical Data and Functional Relationships in Science and Technology, Group 1, Volume 1: Energy Levels of Nuclei, A = 5 to A = 257, ed. by K.H. Hellwege, Springer Press, Berlin, 1961
10. Ortec Instruction Manual, Surface Barrier Detectors, ORTEC, Oak Ridge, Tennessee
11. Leighton, R.B., Principles of Modern Physics, McGraw-Hill Book Co., New York, 1959

PART III

DESIGN STUDY FOR AN X-RAY EXPERIMENT USING A PROPORTIONAL COUNTER

I. THE DETECTOR

The primary purpose of the Grand Tour X-ray Experiment described in this report is to measure the spectrum and time variations of auroral zone x-rays in the range 2-30 keV, and the size and location of the auroral zones of Jupiter and other outer planets. The secondary purpose is to measure the spectra of cosmic x-ray sources and their time variations.

This design study is based on the Reuter-Stokes proportional counter RSG-77 (Figure 1) filled to 1 atmosphere with 97% Xenon, 3% CO_2 , and with a 5 mil Beryllium window. This detector must be collimated, both to avoid the problem of source confusion while viewing an x-ray source, and to provide a characteristic response pattern which will allow the angular size of an x-ray source to be measured. The first requirement is satisfied by rough collimation to a field approximately $5^\circ \times 5^\circ$. In order to measure the size of Jupiter's auroral zones before the spacecraft enters the magnetosphere (and the detector background counting rate increases drastically), much finer collimation is needed: since the Jovian magnetosphere probably extends out to $50 R_J$ in the solar direction, Jupiter will subtend only about 1° when the spacecraft enters the magnetosphere, and collimation down to $\sim 1/10^\circ$ will be necessary. This suggests the use of two collimators; a simple slat collimator for the $5^\circ \times 5^\circ$ field, and a wire grid modulation collimator for the measurement of angular sizes (Figure 2). Consider first the slat collimator, which divides the active area of the proportional counter into an array of squares. If there are n slats/unit length, and their height is h , then each square is collimated to an angle

$\theta = \tan^{-1}(1/2nh)$. Since there are $(n\ell+1)$ slats along the length each having dimensions $w \times h$, and $nw+1$ slats along the width, each having dimensions $\ell \times h$, the total area of the slats is $(n\ell + 1)wh + (nw + 1)\ell h = 2n\ell wh + h(w + \ell) = \left(\frac{\ell w}{\tan\theta}\right) + \left(\frac{w + \ell}{2n \tan\theta}\right)$. Thus, for a given proportional counter (ℓ, w) and collimation angle θ , the minimum total area of slats is obtained for the maximum n . A minimum total area is desirable not only because it minimizes the weight, but also because it keeps the mass in front of the active area down, thus minimizing scattering into the proportional counter.

For the RSG-77, a natural choice for n is $1/1.14$ cm since it allows the collimator slats to be attached to the Beryllium window support structure. Thus for $\theta = 5^\circ$, $h = (2n \tan\theta)^{-1} = 5$ cm, and the total area is $A = 757 \text{ cm}^2$.

Referring to the modulation collimator response pattern shown in Figure 2, we see that if the characteristic angle $\varphi = 1/5^\circ$, a distant point source transiting the collimator will cause the proportional counter to go from a maximum to a minimum count rate in $1/10^\circ$. It follows that, when the x-ray source begins to deviate from a point source and subtends an angle of $1/10^\circ$, the response pattern will start to change noticeably. Figure 3 shows the efficiency of tungsten wire for stopping x-rays; choosing 8 mil wire, and noting from Figure 2 that the wire spacing should be approximately equal to the wire diameter in order to block the x-rays coming from angles $\frac{1}{2}\varphi$, $\frac{3}{2}\varphi$, etc., the height of the collimator $b = a/\tan\varphi = 6.1$ cm. Although the modulation collimator is shown in Figure 2 as a separate unit, it could be incorporated into the slat collimator to save space and weight.

It will be assumed that all interactions in the proportional counter which are not in the 2-30 keV energy range, as well as interactions in the slat collimator, if it is active, will give rise to an anticoincidence signal. (An active "slat" collimator might consist, for example, of a Cesium Iodide slab, viewed by PM tubes, with an array of cylindrical holes leading to the proportional counter.) In addition, interactions in the proportional counter which are in the 2-30 keV window, but are not caused by the x-ray source being viewed, will contribute to the background counting rate. The relative importance of these two effects is as follows. Suppose that an x-ray source, whose true strength is S counts/sec, must be detected in the presence of a background count rate whose true strength is B counts/sec. The detector dead time is bt , where b is the number of interactions/sec which produce an anticoincidence pulse, and t is the length of the gate signal for such a pulse. Then, in a time interval T , $ST - STbt$ counts are collected from the source, and $BT - BTbt$ from the background. The source may be considered to be detected if $ST(1-bt) \geq 3\sigma_{\text{bkgd}} = 3\sqrt{BT(1-bt)}$. Thus $T \geq \frac{9B}{S^2(1-bt)}$, and the factor $B/(1-bt)$ determines the time needed to detect a given source at a 99% confidence level.

Figure 4 shows the x-ray absorption coefficient, μ , for Xenon, versus x-ray energy.^{1,2} It is important to note that, up to an energy of approximately 300 keV, the photoelectric absorption coefficient is much greater than the Compton coefficient; this means that up to 300 keV, if an x-ray interacts at all in the proportional counter, it will most probably interact photoelectrically, leaving all of its energy. Thus x-rays in the energy range 30-300 keV which are incident upon the detector will contribute to the anticoincidence count rate b , rather

than the background count rate B.

This is shown in greater detail in Figure 5, which gives, for the RSG-77 counter, the probabilities of various types of interactions. The top graph (Δ) gives the probability of either a photoelectric or a Compton interaction; that is (probability of no interaction in .005" Beryllium) \times (probability of interaction in 1" Xenon at STP) = $\exp(-\mu_{Be} x_{Be}) [1 - \exp(-\mu_{Xe} x_{Xe})]$, where μ_{Be} and μ_{Xe} are the attenuation coefficients for Beryllium and Xenon, and $x_{Be} = .005" = 9 \times 10^{-3} \text{ g/cm}^2$, $x_{Xe} = 1" = 1.37 \times 10^{-2} \text{ g/cm}^2$. The lower graph gives the probability that a photon, if it interacts, will leave between 2 and 30 keV in the detector. In the energy range 2-30 keV, this is the same as the top graph. Above 30 keV, this is

$$\begin{aligned} & (\text{Probability of interaction of any kind}) \times \frac{\text{Cross-section for transferring} \\ & \quad \text{2-30 keV to electrons}}{\text{Total cross-section}} \\ & = \exp(-\mu_{Be} x_{Be}) [1 - \exp(-\mu_{Xe} x_{Xe})] \frac{1}{\sigma_{\text{total}}} \int_2^{30} \frac{d\sigma_{\text{Compton}}}{dT} dT \end{aligned}$$

where σ_{total} is the total cross-section for a photon interaction of any kind, and $d\sigma_{\text{Compton}}/dT$ is the differential Compton cross-section for a Compton interaction which leaves the electron with an energy $T \rightarrow T + dT$; this integral was done numerically, using the graphs of Nelms.³ Thus the lower graph gives the probability that an incoming photon contributes to the background rate B, while the difference between the top graph and the lower graph gives the probability that an incoming photon contributes to the anticoincidence rate b; this latter probability is zero for energies 2-30 keV and to a good approximation, equal to the top graph for other energies.

In the following sections the counting rates b and B will be determined for this detector; it is convenient to distinguish between two different types of interactions.

1. Counting rates through the forward aperture, caused by particles and photons which enter the detector after passing through the two collimators.
2. Leakage counting rates, caused by photons and particles which originate outside the angles of collimation, but "leak" through the collimator or the sides of the proportional counter.

II. BACKGROUND COUNTING RATES THROUGH THE FORWARD APERTURE

A. Diffuse Cosmic X-ray Flux

The spectrum of the diffuse flux is⁴

$$\begin{aligned}\frac{dN}{dE} &= 10 E^{-1.5} / \text{cm}^2 \text{ sec sr keV}, 1 < E < 10 \text{ keV} \\ &= 16.8 E^{-1.75} / \text{cm}^2 \text{ sec sr keV}, 10 < E < 40 \text{ keV} \\ &= 128 E^{-2.3} / \text{cm}^2 \text{ sec sr keV}, 40 < E < 1000 \text{ keV}\end{aligned}$$

This spectrum is plotted in Figure 6, along with

1. the product of the spectrum and the probability of either a photoelectric or Compton interaction (top graph of Figure 5), and
2. the product of the spectrum with the probability of an interaction which leaves 2-30 keV (lower graph of Figure 5).

Integration of these two graphs gives

1. $7.15/\text{cm}^2 \text{ sec sr}$, the flux which produces the 2-30 keV background counting rate, and
2. $.162/\text{cm}^2 \text{ sec sr}$, the flux which produces the >30 keV anticoincidence counting rate.

Using a total effective area of 39.2 cm^2 for the RSG-77, and a field of view of $5^\circ \times 5^\circ = 7.6 \times 10^{-3} \text{ sr}$, and noting that the modulation collimator obscures half of the counter's effective area, the geometrical factor relating flux to count rate becomes $.149 \text{ cm}^2 \text{ sr}$ for the 2-30 keV background count rate. (Although the modulation collimator becomes transparent at energies above 30 keV, the contribution to the 2-30 keV count rate from fluxes over 30 keV is negligible.) Thus $B = 1.06 \text{ counts/sec}$.

Since the anticoincidence count rate is caused by photons with energies greater than 30 keV, an upper limit to this counting rate may be made by considering the modulation collimator to be transparent; the geometrical factor is therefore $.398 \text{ cm}^2 \text{ sr}$, and the count rate is $b = 6.45 \times 10^{-2} \text{ counts/sec}$.

III. LEAKAGE FLUXES

A. RTG Gamma Rays

The spectrum of RTG gammas is shown in Figure 7; this is the spectrum at 3 ft, 0° from the RTG given by Noon et al.⁵, multiplied by 3 and extrapolated to 13 ft, to give the effect of 3 RTGs assuming no matter exists between the RTG and the x-ray experiment. To obtain the counting rates caused by this flux, consider first the effect of the orientation of the detector to the RTG (Figure 8). To

a first approximation, there can be three orientations:

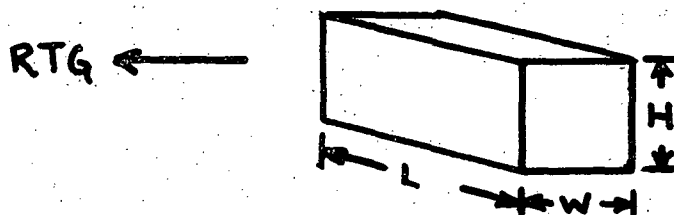


Figure 8

1. The side $H \times L$ faces the RTG; photon path length through counter is W . Count rate $\propto HL [1 - \exp(-\mu W)]$.
2. The side $H \times W$ faces the RTG; photon path length L . Count rate $\propto HW [1 - \exp(-\mu L)]$.
3. The side $L \times W$ faces the RTG; photon path length H . Count rate $\propto LW [1 - \exp(-\mu H)]$.

Noting that the RTG gives no flux below 50 keV, and referring to Figure 4, the absorption coefficient for Xenon is 12 g/cm^2 at 50 keV. Using the approximation $1 - e^{-\mu x} \approx \mu x$, it follows that all of the orientations should give approximately the same count rate. As a worst case, the length $L = 6.25 \text{ inches} = 8.55 \times 10^{-2} \text{ g/cm}^2$, so that, at 50 keV $1 - e^{-\mu L} = 1 - e^{-1.02} = .84$, while $\mu L = 1.02$. However, note that since $e^{-x} \geq 1 - x$, the use of this approximation will give an upper limit to the counting rate even when it is not a good approximation.

Also plotted on Figure 7 are the products of the RTG flux with the maximum probabilities of Figure 5 for each energy range; thus the $\Delta\Delta$ curve gives the flux responsible for the interactions which leave $>30 \text{ keV}$ with an electron, while the $+++$ curve gives the flux responsible for the 2-30 keV interactions. Integrating these curves, and using the

total active area of the detector, 60.5 cm^2 (since the aluminum support structure is transparent to x-rays), the counting rates are:

$$B = 24 \text{ counts/sec}$$

$$b = 5.3 \times 10^2 \text{ counts/sec}$$

The previous analysis neglects the following possibility.

An electron with energy greater than 30 keV, generated either by a Compton or photoelectric interaction, could leave 2-30 keV in the detector, if its path through the gas were less than its range. This is illustrated in Figure 9, which plots the distance which an electron must travel to deposit 2 and 30 keV, versus electron energy for Xenon at STP. Thus, for example, a 1000 keV electron, traveling 1 cm through the detector would leave a countable energy. On the other hand, it is evident from Figure 7 that the worst offenders by far are the RTG photons in the 100-200 keV energy range, and it will be shown later that these can be shielded against relatively easily.

RTG photons can produce background counts in yet another way, illustrated in Figure 10: an incoming photon can interact in the counter walls, either photoelectrically or Compton scattering, thus producing an electron which can enter the counter gas.

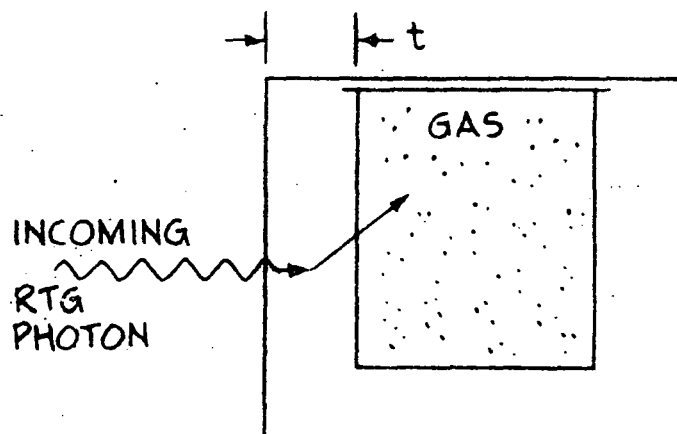


FIG. 10
CROSS SECTION OF PROPORTIONAL CENTER

If the incoming photon has an energy E , it can produce an electron whose maximum energy is $(E - \text{binding energy of atomic electron}) \cong E$, since electron binding energies are small compared to RTG photon energies for materials like Aluminum and Beryllium. Let the range of the electron be $R(E)$ in the counter wall material, and let the wall thickness be t . Then, if the electron is to enter the gas before losing all its energy in the wall, it must be produced a distance $R(E)$ or less from the gas. Thus the incoming photon must not interact in the wall for a distance $t - R(E)$ [probability $\exp(-\mu(E)(t - R(E)))$], and then interact in a distance $R(E)$ [probability $1 - \exp(-\mu(E) R(E))$]. If it is assumed that all such interactions produce a count in the detector, then, as an upper limit the counting rate will be proportional to

$$A e^{-\mu(E)[t-R(E)]} [1 - e^{-\mu(E) R(E)}]$$

where A is the cross-section area presented to the RTG photon flux. A comparison of references 2 and 6 shows that for all types of materials the product $\mu(E) R(E) \ll 1$ at RTG photon energies; thus the counting rate takes the form $Ae^{-\mu(E)t} \mu(E) R(E)$. The graph of Figure 11 gives $\mu(E) R(E) e^{-\mu(E)t}$ versus energy, for 1.15 g/cm^2 of Beryllium (.25" thick) and 1.15 g/cm^2 of Lead (.04" thick). Thus, with the total wall weight held constant, the effect of high Z and low Z materials may be seen on this graph. Consider the Beryllium curve first. At energies over 50 keV, the photoelectric cross-section is negligible, and the product $\mu(E)t$ is small enough so that the exponential term is close to one; thus the expression simply reduces to $\mu(E) R(E)$ (independent of wall thickness). The range $R(E) \propto E^2$, approximately,

while the Compton cross-section decreases slowly with energy; the result is a curve which increases roughly as E^2 , turning over at higher energies.

The case for lead is considerably different; at low energies, the photoelectric cross-section is very large, so the exponential term is small, and the product is small up to approximately 100 keV. Then in the 100-200 keV region the photoelectric cross-section decreases becoming comparable to the Compton cross-section, bringing the exponential term close to 1, and allowing the $\mu(E) R(E)$ term to dominate the expression; since μ for lead is still larger than μ for Beryllium at these energies, the total probability is greater for lead than Beryllium. As the energy increases further, μ for lead becomes about the same as μ for Beryllium (which simply indicates that the Compton cross-section dominates, and there are approximately the same number of electrons/gram for all materials) and the two curves are approximately equal.

Since it is easy to shield against incoming RTG photons with energies below 200 keV, the use of a high Z wall material is not necessary, and Beryllium appears to be the best choice.

RTG photons can produce background counts in yet another manner, illustrated in Figure 12: a photon can pass through the first wall and the gas of the counter without interacting, then backscatter in the second wall and interact in the gas. A rough upper limit to the probability for this type of event is: (Probability that photon of energy E does not interact in the first wall)(Probability that photon of energy E does not interact in gas)(Probability that photon of energy E Compton scatters in second wall)(Probability that 180° backscattered

photon of energy E' interacts in gas). This product is shown in the graph of Figure 13, for 1.15 g/cm^2 Beryllium, and a $1.5''$ path through Xenon at STP.

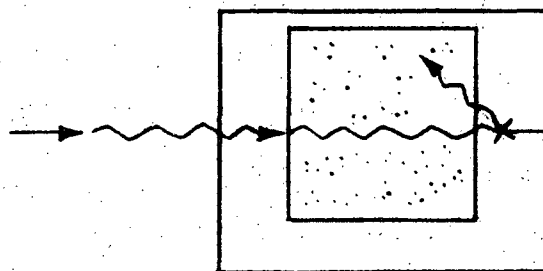


FIG. 12

Finally, the graph of Figure 14 shows the RTG gamma fluxes at the detector (same as Figure 7) and the product of these fluxes with the probabilities of Figure 11 (Beryllium curve) and Figure 13.

Multiplying the total of the two lower curves ($17 \text{ x-rays/cm}^2 \text{ sec}$) by the cross-sectional area (on the order of 40 cm^2) gives an upper limit to $b + B$ of 680 counts/sec . Thus these effects are potentially as serious a problem as direct interactions of the RTG photons.

It seems likely that the propulsion bay of the spacecraft will shield the scan platform from the RTGs; the amount of material present is difficult to estimate, but, as an order of magnitude, 40 g/cm^2 might be used (this corresponds to 15 cm of Aluminum). The effect of Compton scattering of photons is illustrated in the graph of Figure 15; from reference 3, graphs of Compton cross-section versus photon energy were combined to give the average energy of a Compton scattered photon versus distance traveled. At higher energies, where

UPPER LIMIT TO PROBABILITY THAT RTG PHOTON
INTERACTS IN DETECTOR AFTER BACKSCATTERING IN WALL

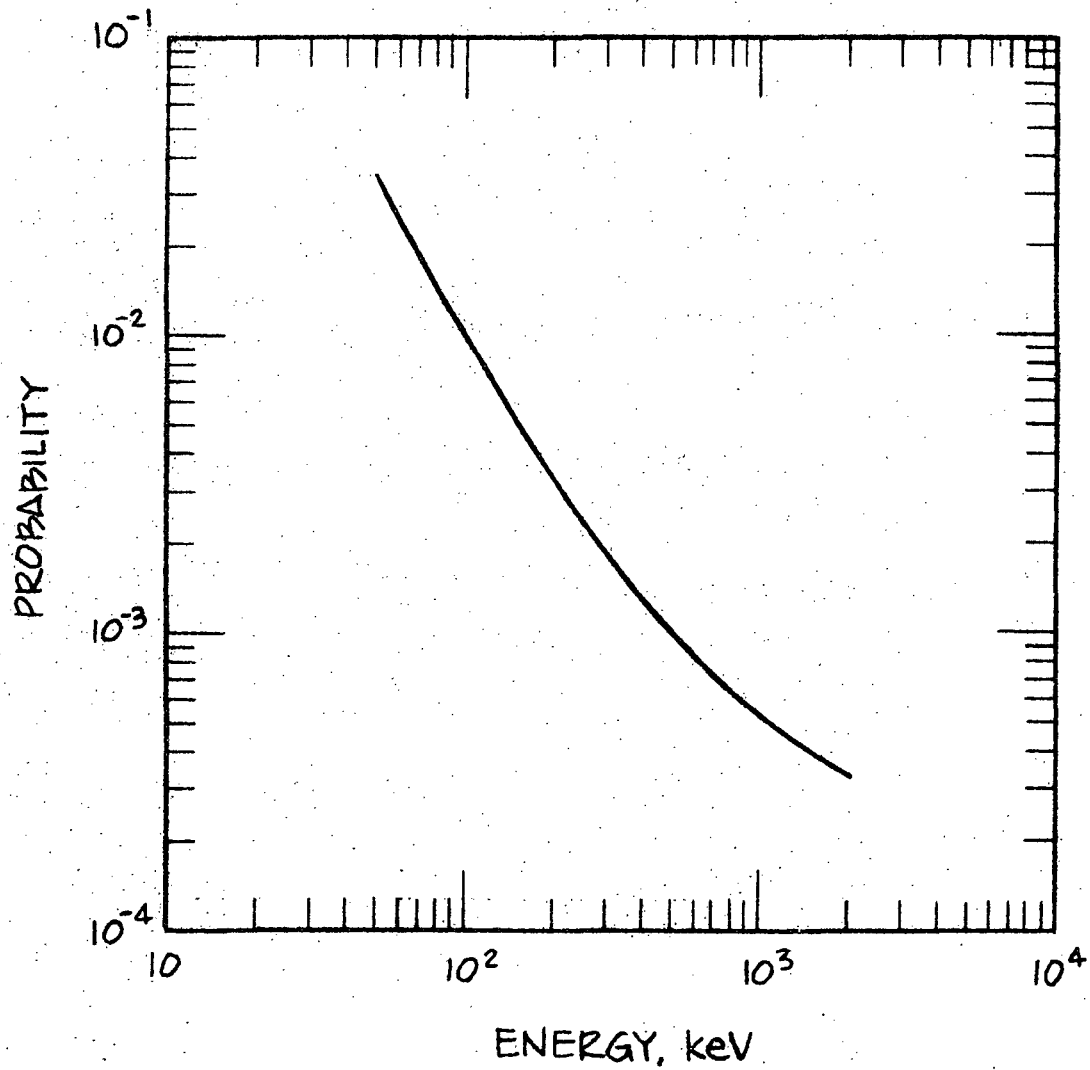


Figure 13

the differential cross-section peaks in the forward direction, the distance traveled is more or less in a straight line; at lower energies the cross-section becomes roughly isotropic, and the distance traveled by the photon is not simply related to the thickness of the shielding material. However, some important features can be deduced from this graph:

1. The 1-2 MeV RTG photons, which are potentially an important source of background, will be reduced in energy to roughly 200-450 keV.
2. The 100-200 keV photons will be reduced in energy to roughly 50-70 keV.

Comparing the photoelectric and Compton cross-sections in Grodstein² it is apparent that Aluminum (in which the photoelectric and Compton cross-sections become equal at 50 keV) will do little to remove the RTG photons, although it will alter the spectrum significantly. To reduce the detector background, a material like Lead will be necessary (where the Compton and photoelectric cross-sections become equal at about 500 keV) or an active collimator.

The percentage of photons which photoelectrically interact in a thickness x g/cm² of Lead is $[\mu_{PE}(E)]/[\mu_{total}(E)](1 - e^{-\mu_{total}(E)x})$ where $\mu_{PE}(E)$, $\mu_{total}(E)$ are the photoelectric and total attenuation coefficients in Lead. From Grodstein² it is clear that for energies below 200 keV this percentage is greater than 75%, for 1 cm (11.34 g/cm²) of Lead, and reduces to about 40% at 500 keV. It seems likely that, after the backscatter calculations have been refined past the upper limit stage, 1 cm of lead will provide the necessary shielding against RTG photons ($1 \text{ cm} \times 40 \text{ cm}^2 \times 11.34 \text{ g/cm}^3 \cong 450 \text{ gm}$).

This may be compared to the weight of an active shield as follows: assume that any interaction in an active shield, either photoelectric or Compton, gives rise to an anticoincidence signal. Then the attenuation factor for photons is $1 - e^{-\mu_{\text{total}} x}$. If we require the same attenuation at 500 keV as for the Lead shield, $1 - e^{-\mu_{\text{total}} x} = .40$ and $\mu x = .51$. For CsI, this would give $x = 7.6 \text{ g/cm}^2$, so the weight would be $7.6 \times 40 \text{ cm}^2 \cong 300 \text{ gm}$. Considering the additional electronics needed for an active shield, it appears that the active and passive shields would have comparable weights. The actual decision between the two will have to await more detailed calculations; it should simply be noted here that shields of moderate weight are capable of reducing the background to an acceptable level.

One final type of RTG gamma interference problem should be considered here: gammas which scatter in the slat collimator and are redirected towards the proportional counter. The geometry for this type of interaction is shown in Figure 16.

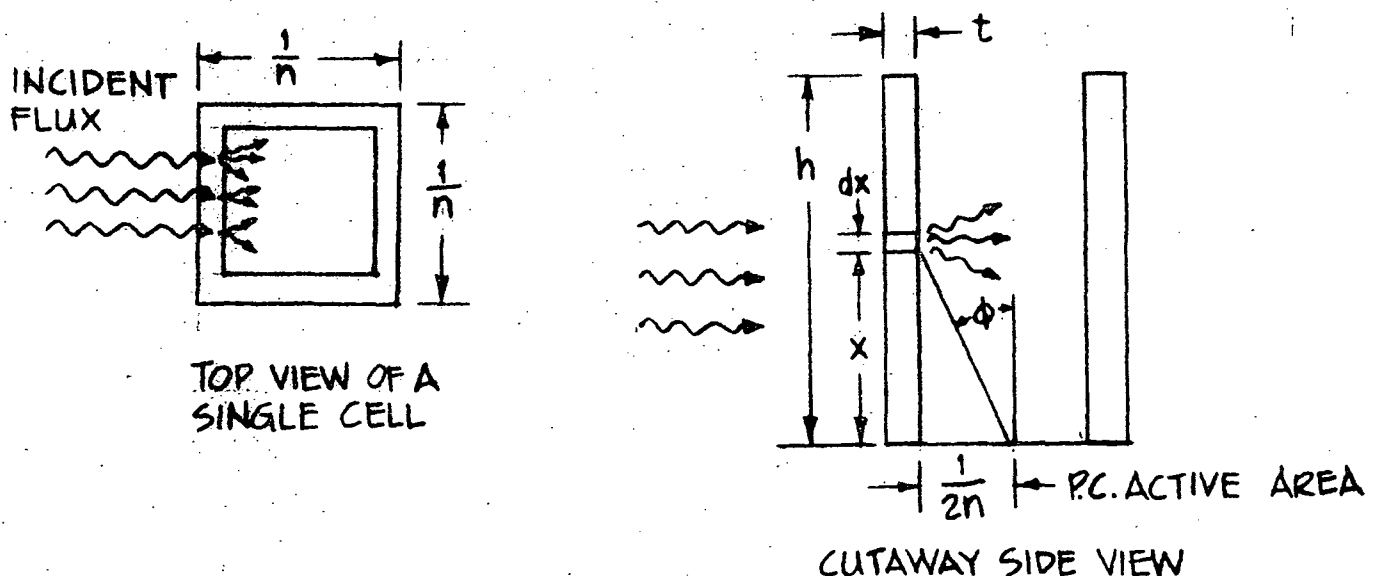


Figure 16

Assume that the scattered photons are emitted isotropically, and let N be the number which escape/cm² sec. Then a thin strip of area dx/n emits Ndx/n photons/sec, and the flux at a distance $\left[x^2 + \left(\frac{1}{2n}\right)^2\right]^{\frac{1}{2}}$ (the distance to the center of the proportional counter cell) is approximately

$$\frac{Ndx}{4\pi n \left[x^2 + \left(\frac{1}{2n}\right)^2\right]} .$$

The proportional counter cell, of area A , presents an effective area $A \cos\phi$ to this flux, and the probability that a photon will interact in the detector is $1 - e^{-\mu_{Xe} d / \cos\phi}$, where d is the detector depth.

Thus, as an upper limit to the contribution from the thin strip, we have

$$\frac{A N dx}{4\pi n \left[x^2 + \left(\frac{1}{2n}\right)^2\right]} \mu_{Xe} d .$$

Integrating over x from 0 to h , this becomes $\frac{A N \mu_{Xe} d}{2\pi} \tan^{-1} 2 nh$.

Using $A = 1.308 \text{ cm}^2$, and $2 nh = 8.75$, this reduces to $.3 N \mu_{Xe} d / \text{sec}$.

Consider next the effect of the orientation of the collimator.

Figure 17 shows the detector after rotation about an axis normal to the Be windows; two sides make an angle θ with the incident flux, and two sides make an angle $90-\theta$; thus if each side has an area a , the number of interactions in the sides is proportional to

$$2a \cos\theta \left(1 - e^{-\mu_{Col} t / \cos\theta}\right) + 2a \cos(90-\theta) \left(1 - e^{-\mu_{Col} t / \cos(90-\theta)}\right) \cong 4a \mu_{Col} t$$

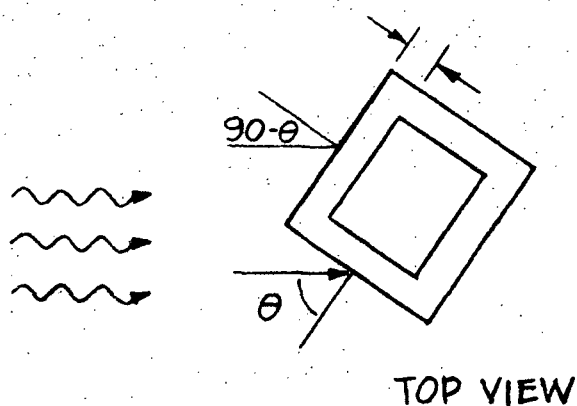


Figure 17

where μ_{Col} is the attenuation coefficient for the collimator material. Thus if the incident RTG flux is $F(E)$ photons/cm² sec in a given energy interval, $N(E) = 4F(E) \mu_{\text{Col}}(E)t$. Since there are 30 cells, the detector counting rate is $36 F(E) \mu_{\text{Col}}(E)t \mu_{\text{Xe}}(E')d$, where E' is the energy of the scattered photon. Using the Xenon interaction probabilities of Figure 5, and choosing E' to be the energy of the 85° scattered photon (i.e., the minimum energy photon, to give the maximum interaction probability), the results are shown in Figure 18. A .02 cm thick (.227 g/cm²) Lead collimator has been assumed. The total counting rates are

$$b = 3.03 \times 10^2 \text{ counts/sec}$$

$$B = 1.22 \text{ counts/sec.}$$

Table I summarizes the effects of RTG gamma rays.

Table I

Source	Diffuse X-rays	Direct Interactions of RTG Gammas	Wall Interactions of RTG Gammas	Collimator Interactions of RTG Gammas
B(2-30)	1.06 c/s	24 c/s	$< 6.8 \times 10^2 \text{ c/s}$	1.22
b(>30)	$6.45 \times 10^{-2} \text{ c/s}$	$5.3 \times 10^2 \text{ c/s}$		3.03×10^2

B. RTG Neutrons: Direct Effects in Proportional Counter

The RTG neutron spectrum is shown in Figure 19; this is the spectrum given by Noon et al.⁵, multiplied by three, and extrapolated to 13 ft, as for the gamma spectrum. The total flux of neutrons is $1.37 \times 10^2/\text{cm}^2 \text{ sec}$. From Hughes,⁷ it is clear that total neutron cross-sections are relatively constant above 10 keV and do not differ considerably from one element to its neighbor; from Walt and Barschall⁸, the total cross-section for Xenon can be estimated at 6.5 barns/atom = $3 \times 10^{-2} \text{ cm}^2/\text{g}$. By the same argument as in section IIIA, the detector orientation does not affect the number of interactions, to a good approximation. Thus, considering the neutrons to be incident on the window of the proportional counter, the number of interactions/sec is

$$1.37 \times 10^2/\text{cm}^2 \text{ sec} \times 58 \text{ cm}^2 \times (1 - e^{-3 \times 10^{-2} \times 10^{-2}}) = 3.3/\text{sec}.$$

The neutron will leave energy with the recoiling Xenon nucleus. From Evans⁹ (p. 412), the maximum energy that can be imparted to a Xenon nucleus by a 7 MeV neutron is about 200 keV. The Xenon nucleus then loses energy both by ionization and nuclear collisions (Rutherford scattering by a screened potential). As the energy lost in the latter process involves no ionization, it is not detected in the proportional counter. From the pulse height defect curves given by Bertolini,¹⁰ it can be estimated that only Xenon nuclei with energies between 100 and 200 keV will leave a countable energy; neutrons capable of transferring this energy must have an energy greater than about 3 MeV, and the total number of neutrons above this energy is about

NEUTRON SPECTRUM AT 13 FT., 0°, FROM 3 2200W (TH) RTG'S

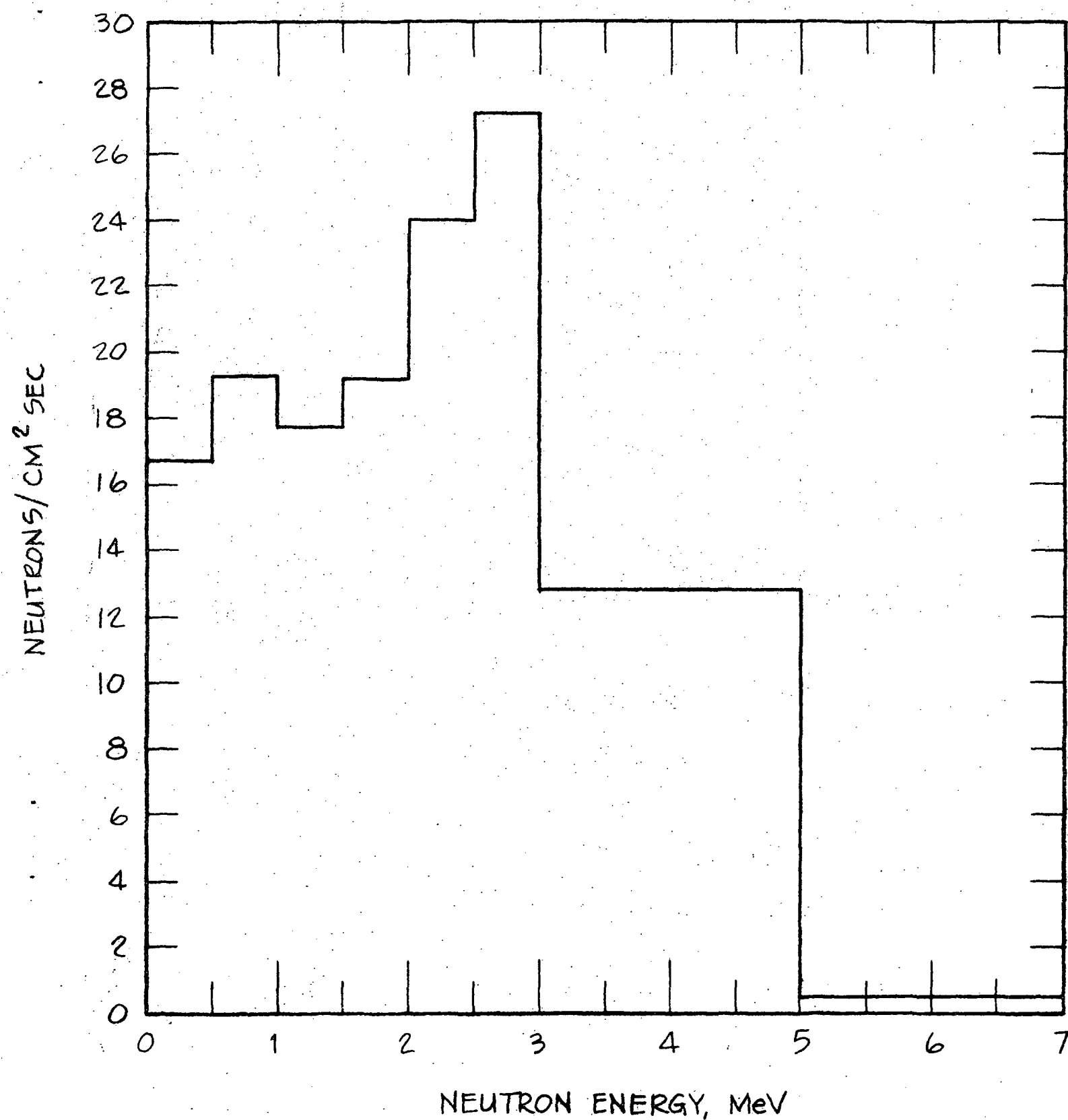


Figure 19

$13/\text{cm}^2$ sec, or $1/10$ the total flux. Thus a rough estimate of the number of counts produced by direct neutron interactions is $.33/\text{sec}$.

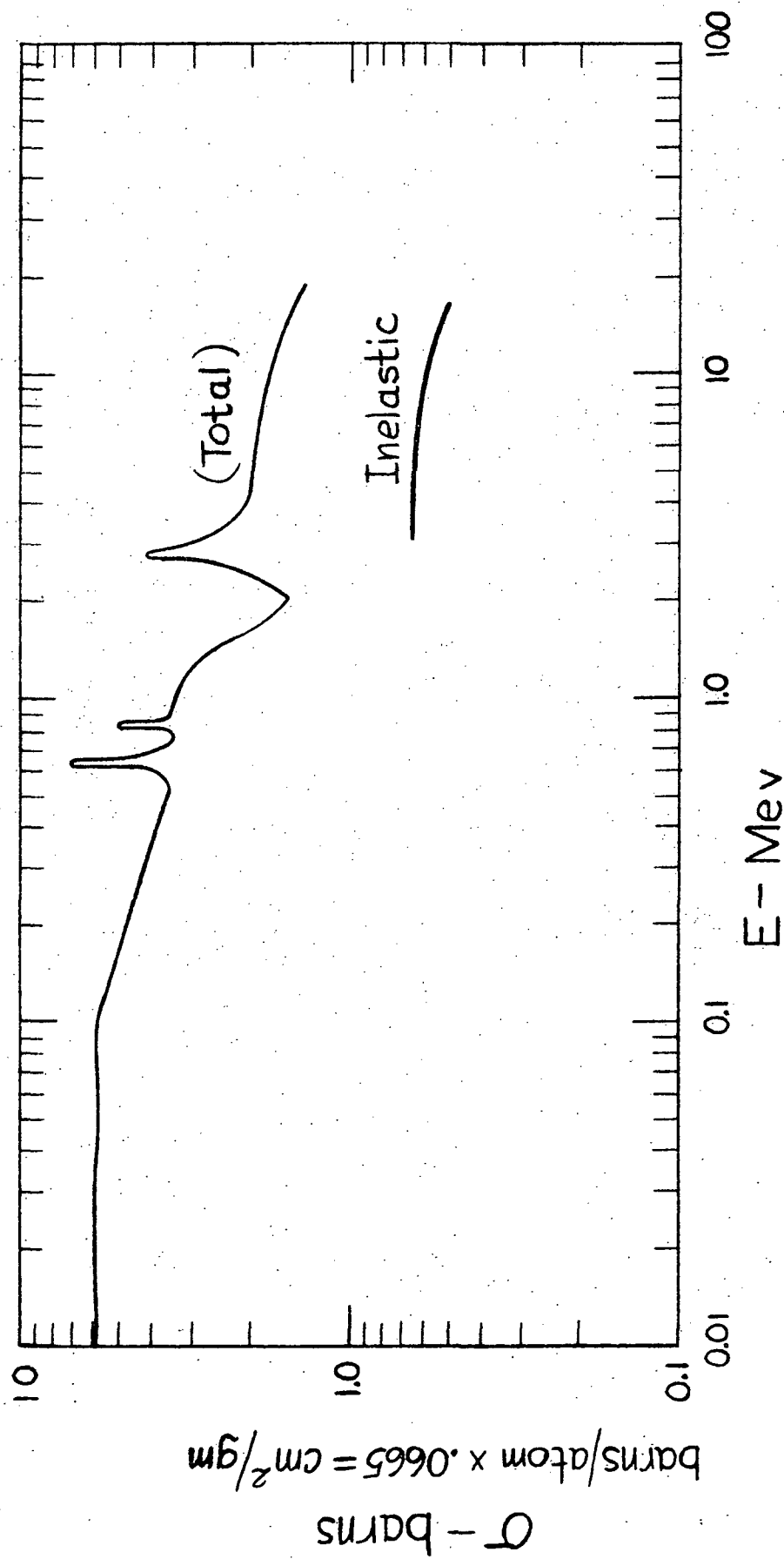
C. RTG Neutrons: Interactions in the Proportional Counter Body

Neutrons interacting in the proportional counter body can produce heavy ions and nuclear gamma rays which can go on to interact in the detector. Suppose, as in section IIIA, that the counter body is 1.15 g/cm^2 Beryllium. The Beryllium cross-section for neutrons is shown in Figure 20. Consider first the background due to Beryllium ions; these will have a range which can be estimated at 10 mg/cm^2 ,¹¹ for 10 MeV ions in Beryllium. Thus an upper limit to the probability of an ion being created and reaching the active volume of the counter is (probability that incoming neutron goes $(1.15-.01) \text{ g/cm}^2$ without interacting)(probability that neutron interacts in $.01 \text{ g/cm}^2$). Taking the cross-section as 6 barns = $.405 \text{ cm}^2/\text{g}$, this is

$$e^{-1.14 \times .405} (1 - e^{-.405 \times .01}) = .63 \times 4.05 \times 10^{-3} = 2.55 \times 10^{-3}$$

Using the total flux of $1.37 \times 10^2 \text{ neutrons/cm}^2 \text{ sec}$ incident on a side of the counter 40 cm^2 in area, the total contribution is $14/\text{sec}$; this represents an upper limit to the sum $b + B$.

The background due to gammas can be estimated by noting that the first excited level of the Be nucleus is about 1.75 MeV ¹² above ground. Thus the probability of a gamma being created and leaving a count in the detector is (probability of neutron interaction in $1.15 \text{ g/cm}^2 \text{ Be}$)(probability that 1.75 MeV gamma interacts in detector).

Cross Sections for Neutrons in Be^9

Again, for the total flux of neutrons incident on a 40 cm^2 side of the detector, an upper limit is

$$b = (1 - e^{-.405 \times 1.15})(5 \times 10^{-4}) 1.37 \times 10^2 \times 40 = (.628)(5 \times 10^{-4}) \\ \times 1.37 \times 10^2 \times 40 = 1.7 \text{ c/s}$$

$$B = (1 - e^{-.405 \times 1.15})(10^{-5})(1.37 \times 10^2) \times 40 = .036 \text{ c/s}$$

D. RTG Neutrons: Effects Due to Interactions in Lead Shields and Collimators

The following neutron reactions can take place in lead for neutrons with energies up to about 7 MeV:

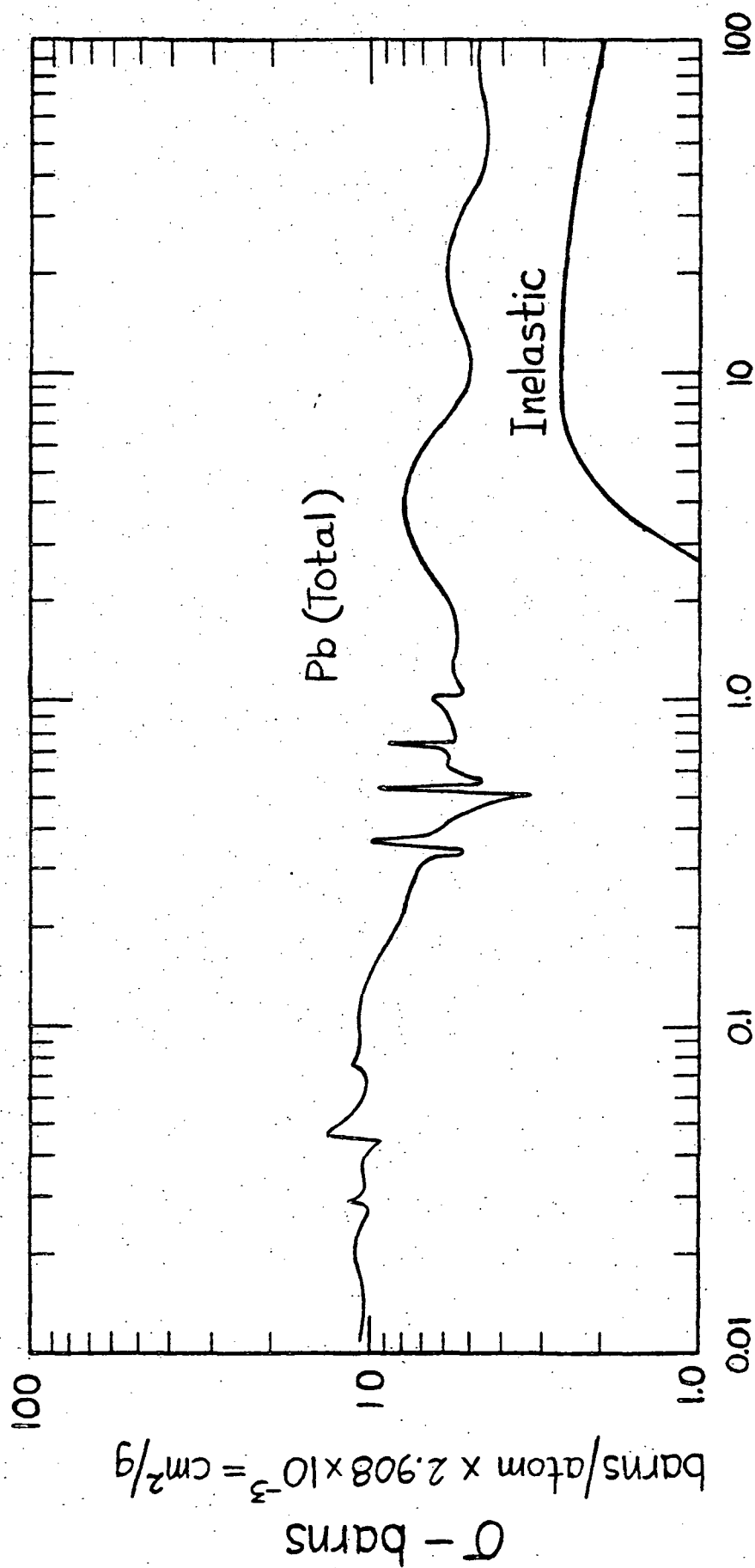
1. $\text{Pb}^{207} (n, n) \text{Pb}^{207}$ (elastic scatter)
2. $\text{Pb}^{207} (n, n') \text{Pb}^{207*}$ (inelastic scatter)

The cross-sections for these reactions are shown in Figure 21.⁷

In the slit collimator, an elastic scatter could direct a neutron towards the proportional counter, while an inelastic scatter could produce a gamma (minimum energy approximately 570 keV^{12}) which could interact in the proportional counter. By the arguments of section IIIA, upper limits to the counting rates produced by these effects are

$$36 F(E) \text{ (Probability of neutron interaction in } .227 \text{ g/cm}^2 \text{ Pb)} \\ \text{(Probability of neutron interaction in } 1.37 \times 10^{-2} \\ \text{g/cm}^2 \text{ Xe) for neutron elastic scattering, and}$$

$$36 F(E) \text{ (Probability of neutron interaction in } .227 \text{ g/cm}^2 \text{ Pb)} \\ \text{(Probability of } 570 \text{ keV gamma interaction in } 1.37 \times 10^{-2} \\ \text{g/cm}^2 \text{ Xe), for neutron inelastic scattering, where } F(E) \\ \text{refers here to the total flux of neutrons.}$$



Cross Sections for Neutron Interactions in Pb^{207} (From (7))

Using 10 barns = $2.91 \times 10^{-2} \text{ cm}^2/\text{g}$ for the cross-section of lead, and 6.5 barns = $3 \times 10^{-2} \text{ cm}^2/\text{g}$ as the cross-section for Xenon, the first count rate is

$$36(1.37 \times 10^2)(1 - e^{-.227 \times 2.91 \times 10^{-2}})(1 - e^{-1.37 \times 10^{-2} \times 3 \times 10^{-2}}) \\ = .0134 \text{ c/s}.$$

And referring to Figure 5 the second is at worst

$$36(1.37 \times 10^2)(1 - e^{-.227 \times 2.91 \times 10^{-2}})(1.3 \times 10^{-3}) = 4.24 \times 10^{-2}$$

If a 1 cm thick lead shield were placed along one side of the counter, as suggested in IIIA, for shielding against gamma radiation, neutrons which scattered inelastically in the lead could give rise to gammas which could then interact in the counter. An upper limit to the probability of this type of interaction is (probability that a neutron interacts in 1 cm = 11.34 g/cm^2 lead)(probability that a 570 keV gamma interacts in proportional counter). Using the total cross-section for lead, and the total neutron flux incident on 40 cm^2 , we have

$$b = 40 \times 1.37 \times 10^2 (1 - e^{-11.34 \times 2.91 \times 10^{-2}})(1.5 \times 10^{-3}) \\ = 5.2 \text{ c/s} \\ B = 40 \times 1.37 \times 10^2 (1 - e^{-11.34 \times 2.91 \times 10^{-2}})(7.5 \times 10^{-5}) \\ = .296 \text{ c/s}$$

E. RTG Neutrons: Effects in a CsI Shield

If an active shield consisting of 7.6 g/cm^2 of CsI is used instead of a lead shield, neutron interactions in the shield will contribute to the

dead time counting rate b . From Hughes,⁷ the cross-section of Iodine can be taken as 6.5 barns/atom and from Walt and Barschall,⁸ the cross-section of Cesium can be estimated at 6.5 barns/atom. The attenuation coefficient for neutrons in CsI then becomes 1.5×10^{-2} cm²/g, and the number of interactions/sec in a 40 cm² shield is

$$b = 40 \times 1.37 \times 10^2 (1 - e^{-7.6 \times 1.5 \times 10^{-2}}) = 5.75 \times 10^2 \text{ c/s} .$$

Table II summarizes the effects of RTG neutrons on the proportional counter.

Table II

Source	b		B
Direct Interaction of RTG Neutron in Proportional Counter	0		.33 c/s
(n, n) Interaction in PC Body	14/sec		
(n, γ) Interaction in PC Body	1.7 c/s		.036 c/s
Neutron Interaction in Lead Collimator	5.58×10^{-2} c/s		
Neutron Interaction in Lead Shield	5.2 c/s		.296 c/s
Neutron Interaction in CsI Shield	0		5.75×10^2

F. Diffuse Cosmic X-ray Flux Leakage

The photons of the diffuse cosmic x-ray flux can "leak" through the slat collimator at angles greater than 5° (it is assumed here that the sides and bottom of the proportional counter will be surrounded by several g/cm^2 of electronics and mechanical structures, minimizing leakage through these areas). Assuming that the slat collimator is made of $.227 \text{ g/cm}^2$ lead (section IIIA), and referring to Grodstein² it is clear that this collimator is at least 90% efficient up to 40 keV. Integrating the curves of Figure 6 above 40 keV, and assuming that the entire top of the counter ($\sim 40 \text{ cm}^2$) is exposed to $2\pi \text{ sr}$, (geometrical factor $40\pi \text{ cm}^2 \text{ sr}$), the upper limits

$$b = 60 \text{ cm}^2 \times \pi \text{ sr} \times 10^{-1} / \text{cm}^2 \text{ sec sr} = 18/\text{sec}$$

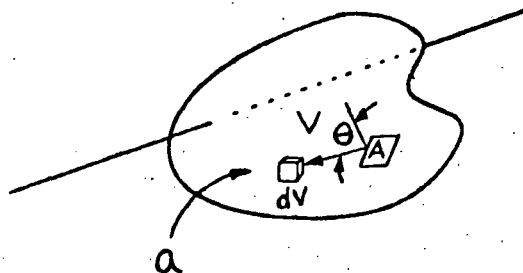
$$B = 60 \text{ cm}^2 \times \pi \text{ sr} \times 10^{-3} / \text{cm}^2 \text{ sec sr} = .18/\text{sec}$$

G. Cosmic Ray Interactions in the Proportional Counter

A minimum ionizing proton (energy greater than about 1 GeV) will lose roughly 2 MeV/g/cm^2 in Xenon. Paths from 0 to 7 inches are possible, so energy losses of 0 to 200 keV can occur. Using a flux of $1 \text{ cosmic ray/cm}^2 \text{ sec sr}$ above 1 GeV, and considering the entire area of the counter (200 cm^2) to be exposed to 2π , the number of cosmic rays traversing the counter is 628/sec. Rise time discrimination must therefore be used to minimize the effects of cosmic rays.

H. Cosmic Ray Interactions in the Spacecraft

If N is the flux of cosmic rays ($\text{cm}^{-2} \text{ sec sr}$), $N \pi a$ cosmic rays/sec will be incident on the area a bounding a volume V .



If the volume V has a mass W , a typical path through the volume has a thickness $W/a \text{ g/cm}^2$. Using a mean free path of 80 g/cm^2 for cosmic rays, the probability of an interaction is $1 - e^{-W/80a}$. Rough estimates give $W = 6.5 \times 10^5 \text{ g}$ and $a = 6 \times 10^4 \text{ cm}^2$ for the Grand Tour spacecraft, so $W/a = 11 \text{ g/cm}^2$, and the probability is approximately $W/80a$ in this case. Thus the number of interactions per second is $N \pi a W/80a = N \pi W/80$. Assuming uniform production of gammas throughout the volume, and assuming that each interaction produces a gamma ray, then a small volume dV produces

$\frac{N \pi W}{80} \frac{dV}{V} \gamma/\text{sec}$. The flux at a detector a distance r from dV is

$\frac{N \pi W}{80} \frac{dV}{V} \frac{1}{4 \pi r^2} \gamma/\text{cm}^2 \text{ sec}$. A detector of area A , whose normal makes an angle θ with r , will intercept

$$\frac{N \pi W}{80} \frac{dV}{V} \frac{1}{4 \pi r^2} A (1 - e^{-\mu x / \cos \theta}) \cos \theta \approx \frac{N \pi W}{80} \frac{dV}{V} \frac{A \mu x}{4 \pi r^2} \gamma/\text{sec}.$$

Thus the number of counts/sec due to the entire volume is

$$\frac{N\pi W}{80} \frac{1}{V} \frac{A\mu x}{4\pi} \int \frac{dV}{r^2}$$

Evaluation of this integral for simple geometries (spheres and cylinders) shows that it is of the order $4\pi r$, where r is a characteristic dimension of the object. Taking the case of a sphere, with the detector at the center, there will be

$$\frac{N\pi W}{80} \cdot \frac{1}{\frac{4}{3}\pi r^3} \cdot \frac{A\mu x}{4\pi} \cdot 4\pi r = \frac{3N\pi}{80} \left(\frac{W}{a}\right) A\mu x$$

Using $N = 1$, $W/a = 11 \text{ g/cm}^2$, this becomes $1.2 A\mu x$ counts/sec.

Taking $A = 40 \text{ cm}^2$ and $\mu x = 1$ for an upper limit, we get 48 counts/sec for an upper limit to $b + B$.

I. Summary

The following table summarizes the background effects from various sources.

Table IV

Source	b	B
Diffuse x-rays (IIA)	.064/sec	1.06/sec
Direct Interactions of RTG Gammas (IIIA)	530/sec	24/sec
Interaction of RTG Gammas in PC Walls (IIIA)	680/sec	
Interaction of RTG Gammas in Collimator (IIIA)	303 c/s	1.22 c/s
Direct Interaction of RTG Neutrons in PC (IIIB)	0	.33 c/s
(n,n) Interaction in PC Body (IIIC)	14 c/s	
(n, γ) Interaction in PC body (IIIC)	1.7 c/s	.036 c/s
Neutron Interaction in lead Collimator (IIID)	.055 c/s	
Neutron Interaction in lead Shield (IIID)	5.2 c/s	.296 c/s
Neutron Interaction in CsI Shield (IIIE)	575 c/s	0
Diffuse X-ray Leakage (IIIF)	18 c/s	.18 c/s
Direct Interaction of Cosmic Rays (IIIG)	628 c/s	
Cosmic Ray Interaction in Spacecraft (IIIH)	48 c/s	

IV. CONCLUSION

The most serious background problem is caused by RTG gamma radiation. Direct interactions of RTG gammas can be reduced by active or passive shielding of the counter, as well as pulse risetime analysis on the counter output; this technique can reduce the background by up to 90%, while retaining 80% of the x-ray efficiency.^{13,14}

The problem of gamma interactions in the proportional counter body can be solved by the use of multiwire proportional counters: an array of anode wires is placed inside the counter next to the walls, and pulses are accepted from the central anode wire in anticoincidence with the wire array. Thus electrons originating in the counter walls are gated out. This technique has been investigated by Charpak *et al.*,¹⁵ Borkowski and Kopp,¹⁶ and Bouclier *et al.*¹⁷ In particular, Charpak *et al.* have shown that wire spacings down to 1 mm are possible with each wire behaving as a separate proportional counter, and with no sacrifice in energy resolution. Multiwire counters will also be used on the HEAO spacecraft.

We conclude that, using currently produced proportional counters, in conjunction with proven anticoincidence techniques, an x-ray detector is capable of operating reliably on the Grand Tour spacecraft.

REFERENCES

1. Kaelble, E.F., Handbook of X-rays, McGraw-Hill, New York, 1967
2. Grodstein, G.W., X-ray Attenuation Coefficients from 10 keV to 100 MeV, NBS Circular, 583, 1957
3. Nelms, A.T., Graphs of the Compton Energy-Angle Relationship and the Klein-Nishina Formula from 10 keV to 500 MeV, NBS Circular 542, 1953
4. Silk, J., Diffuse Cosmic X- and Gamma Radiation: The Isotropic Component, Space Sci. Rev., 11, 671, 1970
5. Noon, E.L., G.H. Anno, and M.A. Dore, Nuclear Radiation Sources on Board Outer Planet Spacecraft, IEEE Transactions on Nuclear Science, NS-18, (5), 1971
6. High Energy Particle Data, UCRL 2426, Vol. II (1966 Rev.)
7. Hughes, D.J., Neutron Cross Sections, Brookhaven National Laboratory Report BNL-325, 1955 and 1958 (U.S. Government Printing Office, Washington, D.C.)
8. Walt, M. and H.H. Barschall, Scattering of 1 MeV Neutrons by Intermediate and Heavy Elements, Phys. Rev., 93, 5, 1954
9. Evans, R.D., The Atomic Nucleus, McGraw-Hill, New York, 1955
10. Bertolini, G., Semiconductor Detectors, North-Holland Publ. Co., Amsterdam, 1968
11. Whaling, W., The Energy Loss of Charged Particles in Matter, Handbuch der Physik, Vol. 34, 1958
12. Landolt-Bornstein, H.H., Numerical Data and Functional Relationships in Science and Technology, Group 1, Volume 1: Energy Levels of Nuclei, A = 5 to A = 257, ed. by K.H. Hellwege, Springer Press, Berlin, 1961
13. Gorenstein, P. and S. Mickiewicz, Reduction of Cosmic Background in an X-ray Proportional Counter Through Risetime Discrimination, Rev. Sci. Instru., 39, 6, 1968
14. Culhane, J.L., and A.C. Fabian, Circuits for Rise Time Discrimination in Proportional Counters, presented at IEEE Nuclear Science Symposium, San Francisco, California, 1971

15. Charpak, G., R. Bouclier, T. Bressani, J. Favier, and C. Zupancic, The Use of Multiwire Proportional Counters to Select and Localize Charged Particles, Nuc. Instru. and Methods, 62, 262, 1968
16. Borkowski, C.J. and M.K. Kopp, New Type of Position Sensitive Detectors of Ionizing Radiation Using Risetime Measurement, Rev. Sci. Instru., 39, 10, 1968
17. Bouclier, R., G. Charpak, Z. Dimcovski, G. Fisher, and F. Sauli, Investigation of Some Properties of Multiwire Proportional Chambers, Nuc. Instru. and Methods, 88, 149, 1970

PART IV

SUMMARY AND ACKNOWLEDGMENTS

The present best choice of instrument thus appears to be:

1. Two separate multiwire proportional counters for redundancy.
2. Passive collimation to restrict the field to $\sim 5^\circ$, wire-grid modulation collimation to $\sim 0.1^\circ$ angular resolution.
3. No active shielding system around the counter body is required.
4. Light passive shielding around any portion of the counter body exposed to space to absorb most of the cosmic x-ray background.

Instruments of this description are well known in the laboratory and are widely used in x-ray astronomy on rockets and will soon be used on satellites such as OSO and HEAO. Development of the planetary x-ray experiment is therefore largely accomplished.

ACKNOWLEDGMENTS

The laboratory measurements and much of the detailed design study was carried out by Dr. Kevin Hurley of the Space Sciences Laboratory, University of California, Berkeley. This work was supported by the NASA under grant NGR-05-003-458.